# SPINTRONIC DEVICES BASED ON METAL DICHALCOGENIDES MATERIALS

WONG WANG CHEUNG

M.Phil

The Hong Kong Polytechnic University

2018

**The Hong Kong Polytechnic University**

**Department of Applied Physics**

# Spintronic Devices Based on Metal Dichalcogenides Materials

Wong Wang Cheung

A thesis submitted in partial fulfillment of the requirements

for the degree of Master of Philosophy

**March 2017**

THE HONG KONG POLYTECHNIC UNIVERSITY

# Certificate of Originality

I hereby declare that this thesis is my own work and that, to the best of my knowledge and belief, it reproduces no material previously published or written, nor material that has been accepted for the award of any other degree or diploma, except where due acknowledgement has been made in the text.

_____ (Signature)

Wong Wang Cheung (Name of candidate)

# Abstract

Two dimensional (2D) materials such as graphene or $MoS_2$ are well-suited for use in electronic devices. For example, the high on-off ratio of transistors based on 2D materials has drawn much attention as the replacement of silicon transistors. Besides, graphene also demonstrates outstanding spintronic properties, with long spin lifetime (1-6 ns at 4 K) and spin diffusion length (3-12 μm at 300 K) as compared with conventional semiconductors (GaAs, highly doped Ge) or metals (Cu, Al).[1, 2] As a result, graphene-based spin logic devices have been proposed.[3]

Compared with graphene, $MoS_2$ is a 2D material that is more often investigated for optoelectronics applications. At the same time, $MoS_2$ also shows special spin-related properties. Due to the symmetry breaking that exists in thin $MoS_2$, a long spin lifetime in the order of nanoseconds was predicted.[4] $Fe/MoS_2/Fe$ magnetic tunnel junctions were predicted to demonstrate large magnetoresistance ratio (MR) of 300% according to fully atomistic first-principle transport calculations, which was attributed to an efficient spin injection due to the strong hybridization between iron and sulphur atoms.[5] Moreover, planar

(edge-contacted) Fe/$MoS_2$/Fe junctions were estimated to yield MR of 150% using non-equilibrium Green's function calculations. Experimental results of NiFe/$MoS_2$/NiFe junctions, however, showed a mere MR of 0.73% and was significantly different from the calculation results.[6]

Typically, the $MoS_2$ spacers in tunnel junctions were fabricated by wet transfer *ex situ*, which may trap contaminants or induce inhomogenous coverage of electrodes surfaces, and could also lead to oxidation of electrodes during the transfer process. These unwanted artifacts could decrease the quality of contact interfaces. Previous investigations on boron nitride magnetic tunnel junctions with the spacer layer grown *in situ* by chemical vapour deposition (CVD) showed an order of magnitude improvement in the MR compared with wet-transferred spacers, [7, 8] highlighting the importance of the contact quality on the junction performance.

In this thesis, I fabricated $La_{0.7}Sr_{0.3}MnO_3$ (LSMO)/$MoS_2$/NiFe vertical spin valves, with the $MoS_2$ spacer layer prepared by magnetron sputtering. The choice of bottom electrode is based on the chemical stability of LSMO against reaction with oxygen. Sputtering process eliminates contaminants and incomplete

coverage of bottom electrodes by $MoS_2$, thus improving the quality of contacts between $MoS_2$ and the magnetic electrodes.

In this project, four-point electrical measurements were used to measure both electrical and transport properties of the devices. LSMO bottom electrodes were deposited by pulsed laser deposition (PLD) on $SrTiO_3$ (STO) substrates. $MoS_2$ thin films were deposited on LSMO by direct RF magnetron sputtering at room temperature to suppress sulphur vaporization. The $MoS_2$ layer was then post-annealed at 450ºC under a nitrogen atmosphere of 1 atm. by rapid thermal annealing to enhance the crystallinity. NiFe top electrode and Au capping layer were finally deposited by electron-beam evaporation.

$MoS_2$ films sputter-deposited on LSMO showed characteristic $E_{2g}$ and $A_{1g}$ vibrations of $MoS_2$ in Raman spectroscopy. The result suggested that crystalline $MoS_2$ was successfully grown on LSMO. Using this sputtering method, $MoS_2$ films could be grown on various substrates at lower temperatures as compared with CVD. MR measurement of such $MoS_2$-spacer spin valve showed 0.8% MR at 20 K. The results suggested a method to fabricate 2D material-based spintronic and electronic devices with reliable contacts.

# Acknowledgements

I would like to express my gratitude to my supervisor Dr. C. W. Leung for all the supports, assistance and guidance during the study periods. Special thanks should be devoted to Dr. C. L. Mak for his inspiring discussion.

Thanks are extended to Ms. S. M. Ng, Mr. H. F. Wong and Mr. W. F. Cheng for their assistances and helpful suggestions.

I would also like to thank the financial and technical support provided by the Department of Applied Physics and University Research Facility in Materials Characterization and Device Fabrication (UMF) of the Hong Kong Polytechnic University.

Last but not the least, I would like to thank my family and friends for their endless love and support throughout my life.

THE HONG KONG POLYTECHNIC UNIVERSITY

# Table of Contents

# Chapter 1.**Introduction**

## 1.1. **Introduction of spintronics**

Spintronics is a study of controlling the spin degree of freedom in charge carriers. The operation of spintronic devices is based on the interaction between the spin in the carriers and its solid-state environment. There are three key factors that can influence performance of the spintronic devices, namely the effectiveness of polarizing spins (i.e. spin generation), the spin life time (spin retention) in the system and ability to detect spins (spin detection).[9] The first factor is related to generation of non-equilibrium spin population. It can be achieved by transferring the angular momentum from circularly polarized photons to electrons or by passing a current through a spin-polarizing (typically ferromagnetic) electrode. The second factor is caused by the spin relaxation, which is a mechanism for non-equilibrium spin population (non-zero spin polarization) to return to equilibrium. It is mainly related to the spin-orbit coupling which is the interaction of electron spin and the lattice environment. The range of spin relaxation time varies from picoseconds to microseconds in various materials. The final factor is about maximizing the spin signals generated by the nonequilibrium spin population in

the system. Most of the spintronic devices are designed with the goal of increasing the sensitivity of spin detection upon the change of the spin states.

The research on spintronics started with the studies on spin -polarized transport,[10] which gave rise to the abnormal resistance change in ferromagnetic materials. In a ferromagnetic material, charge carriers may carry spins of majority and minority favour, whose magnetic moment directions are parallel and antiparallel to the magnetization direction respectively. Magnon scattering becomes extremely small at low temperatures. At this situation, the two spin channels undergo independent scattering processes. As the result, the resistance of the materials depends on two separate scattering processes (hence named the two current model). Many magnetoresistive phenomena with the resistance change affected by external magnetic fields (magnetic tunnel junction[11, 12] or giant magnetoresistance [13, 14]) could be explained based on this model.

Presently, the applications of spintronics are mostly focused on read heads of hard disks and magnetoresistive random access memories (MRAM). Both of the applications are based on spin transfer torque [15, 16], giant magnetoresistance (GMR)[13, 17, 18], tunnelling magnetoresistance [19, 20]and

spin-valve effects[21, 22]. Recent research focus in the spintronics field include the spin Hall effect, spin generator and spin channel materials.

### 1.1.1. Tunneling magnetoresistance

Tunneling magnetoresistance (TMR) can be observed in magnetic tunnel junctions (MTJ). MTJ investigation started from the research on spin-transport experiment of ferromagnet/insulator/superconductor junctions.[20] The superconductor was used as the spin polarization detector based on the Zeeman-split quasiparticle density of state. This experiment showed that the spin polarization, which was detected from tunneling current through the insulator, could be leaked outside the ferromagnet.

Afterwards, the research on ferromagnet/insulator/ferromagnet (Fe/Ge/Co) junctions started.[23] Cobalt and iron have different coercive fields, and the magnetization directions of Co and Fe layers can achieve parallel or anti-parallel states when the external field is larger or in between the coercive fields of Co and Fe. (Fig. 1.1.1-1) The conductance of the junction will then be varied by the external magnetic field and this phenomenon is called TMR.

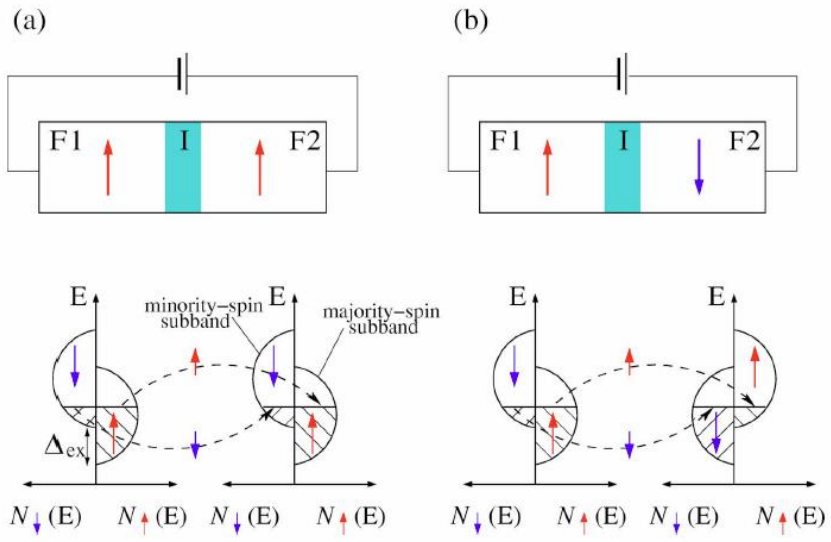


*Fig. 1.1.1-1 Schematics of ferromagnet/insulator/ferromagnet MTJ with spin density for two ferromagnets (F1 and F2) under (a) parallel and (b) anti-parallel state.[9]*

MR ratio is a commonly used parameter to represent the strength of the effect, and is expressed by following equation [9]:

$$MR\ ratio = \frac{R_{anti-parallel} - R_{parallel}}{R_{parallel}} = \frac{G_{parallel} - G_{anti-parallel}}{G_{anti-parallel}} \quad (1)$$

Where $R$ is the resistance and $G$ is the conductance with $G = 1/R$. The subscripts represent the relative magnetization orientation of the two magnetic layers. TMR strength is related to the spin polarization of the two ferromagnetic layers. By the Julliere's model [23], under the approximation that electrons tunnel without spin flip, TMR can express by following equation:

$$TMR = \frac{2P_1P_2}{1 - P_1P_2} \quad (2)$$

where $P_2$ and $P_2$ are the polarizations of two ferromagnet, and the

polarization is expressed by the equation:

$$P_i = \frac{\mathcal{N}_{Ma} - \mathcal{N}_{Mi}}{\mathcal{N}_{Ma} + \mathcal{N}_{Mi}} \quad (3)$$

Where $\mathcal{N}_{Ma}$ and $\mathcal{N}_{Mi}$ are the majority and minority spin-resolved density of states, respectively. However, this model failed to explain the temperature and voltage dependence of TMR [9].

Nowadays, MTJ are widely used in read heads of magnetic hard disks. By rotating the magnetic disk, the magnetic field changes which correspond to the stored data bits of 1 or 0 are read out through the resistance change of MTJ read heads. Recent research has achieved a TMR ratio of 1144% at 4 K.[19]

### 1.1.2. Giant magnetoresistance

Giant magnetoresistance (GMR) was discovered in (001)Fe/(001)Cr superlattices,[17] in which a large resistance drop appeared at large external field. When the external field is greater than saturation field, the magnetization of all Fe layers are aligned along the field direction. In the zero field situation, the magnetization in adjacent Fe layers are aligned in an anti-parallel fashion. The large resistance change can be explained by the two current model.[10] There are

up and down spin currents going through the superlattice. When the Fe layers are in parallel alignment, up spin electrons suffer from little scattering all Fe layers but down spin electrons are strongly scattered. The up spin channel therefore has a lower resistance than the down spin channel, which can be considered as two resistors of high (down spin channel) and low (up spin channel) resistances connected in parallel. For anti-parallel Fe magnetization alignment, both up and down spin electrons have little scattering at the Fe layers with the same magnetization direction but receive strong scattering at opposite magnetization direction layers. Both up and down spin currents have the same resistance. As a result, the parallel state has a smaller resistance. The schematic illustration of this phenomenon is shown in Fig. 1.1.2-1.

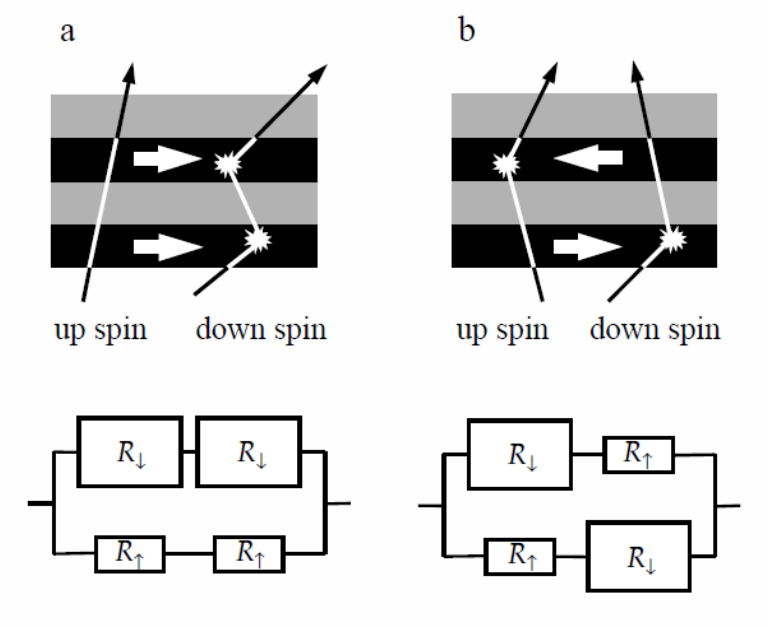


*Fig. 1.1.2-1 Schematic illustrations (upper panels) and equivalent circuit diagrams (lower panel) of GMR in (a) parallel and (b)anti-parallel states [24].*

GMR structures are divided into two types according to the current flow direction: current in plane (CIP) and current perpendicular to plane (CPP) geometries as shown in Fig. 1.1.2-2. The CIP structure is widely used in applications because of the simplicity in device fabrication. On the other hand, the CPP structure shows higher MR ratio than the CIP structure,[25] and the CPP geometry is more suitable for theoretical analysis of GMR or TMR.

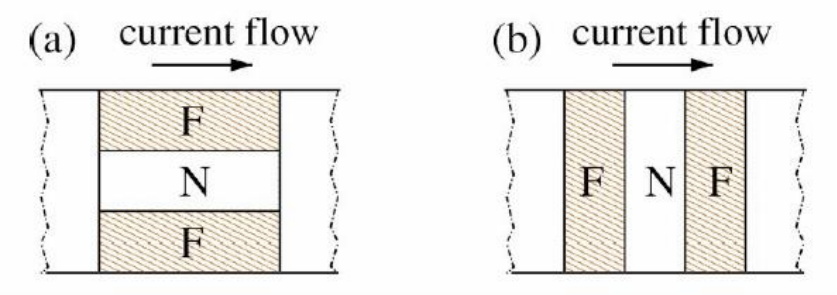


*Fig. 1.1.2-2 Schematic illustration of (a) CIP and (b) CPP measurement geometries [9].*

### 1.1.3. Spin valve structure

The magnetic field required to switch the GMR multilayer structure into parallel state is quite high due to the strong antiferromagnetic coupling between magnetic layers across the non-magnetic spacer. In order to achieve a low magnetic field switching for application purposes, the spin valve structure was fabricated.[18] In this structure, relatively thick Cu was sandwiched between two ferromagnetic layers. An antiferromagnetic film was then deposited on one of the ferromagnetic layers, which was then pinned by the exchange bias coupling at the ferromagnet/antiferromagnet interface. The result of exchange bias is the shift of the hysteresis loop (MH loop) of the pinned ferromagnetic layer. The anti-parallel state can be achieved over a relatively wide field range (Fig. 1.1.3-1).

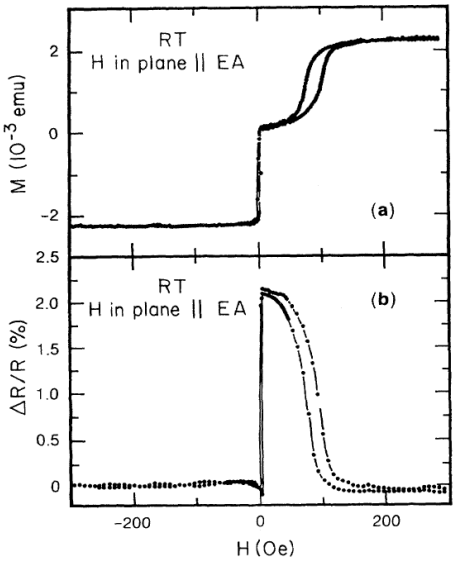


*Fig. 1.1.3-1 Hysteresis loop and MR measurement of NiFe/Cu/NiFe/Ag spin valve device.[18]*

Another type of spin valve does not require the antiferromagnetic layer for exchange bias and achieve antiparallel magnetization of the magnetic layers. It is fabricated by depositing two layers of ferromagnetic materials with large difference of coercivities. The layers with smaller and larger coercivities are called soft and hard layers, respectively. The anti-parallel alignment appears when the applied magnetic field is in between the coercive fields of the two magnetic layers. This kind of structure is called the pseudo spin valve.

A variation of the spin valve structure is to connect laterally separated ferromagnetic electrodes on the substrate surface with a spin-transporting channel material. [21] The device structure is shown in Fig. 1.1.3-2. In this example, Cu

crossbar channel is deposited on two NiFe electrodes with different widths (hence different coercive fields). The current flows from one end of the Cu crossbar and comes out from one of the NiFe electrodes (Py1). The voltage is measured between the other side of Cu crossbar and the other NiFe electrode (Py2). This measurement configuration is called the non-local spin valve.

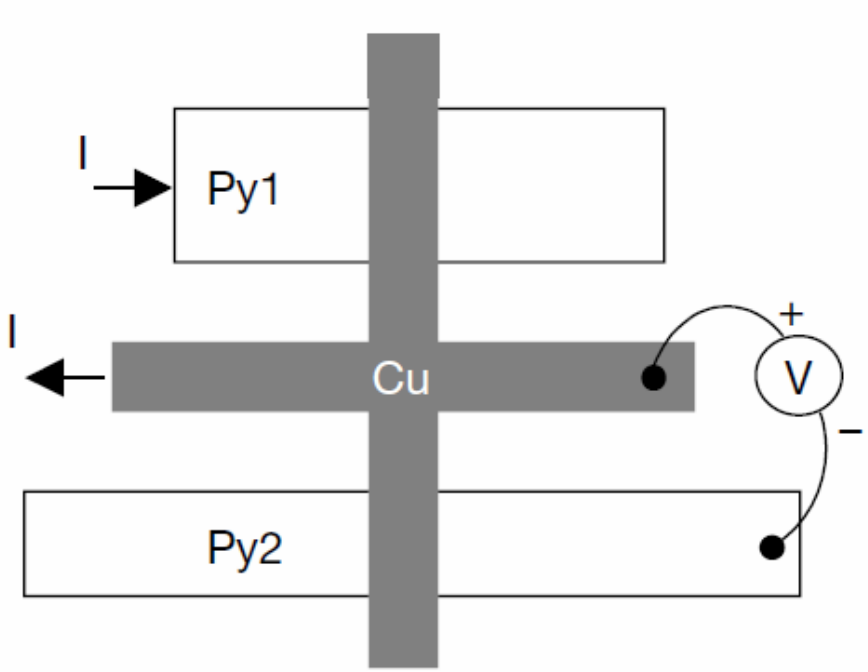


*Fig. 1.1.3-2 Schematic diagram of the non-local lateral spin valve structure [21]*

The resistance measured by the non-local spin valve is not the real resistance because of the position difference of the current flow and voltage measurement. The origin of resistance change in the non-local spin valve is the

spin diffusion in the spin channel materials. The charge carriers become polarized because of the ferromagnetic electrode. The spin-polarized current flow through the spin channel material to the current source terminal. The spin polarized current induces a diffusive spin flow in the channel crossbar, which is independent of the charge current flow. The spin diffusion current induces a voltage difference on the voltage measurement terminals. The voltage depends on the magnetization direction and spin-polarization direction. As the result of different coercive fields of ferromagnetic electrodes, the resistance state is changed when the electrodes shift between parallel and at anti-parallel state. By changing the distance between voltage measurement terminals, the spin signal resistance is varied because of the finite spin diffusion length of the spin channel. Recent researches have identified some long spin life time and long spin diffusion length materials, such as highly doped Si [26], GaAs [27] and graphene [1, 2].

## 1.2. Introduction of two-dimensional metal dichlalcogenides

Two dimensional (2D) materials have drawn great research interests from the start of 21$^{st}$ century. 2D materials are atomically-thick materials from layer-

structured materials. Early calculation results by classical physics of 2D materials showed thermodynamic instability for monolayer form of such materials because the atomic thickness were thought to be thermally unstable. However, using the harmonic approximation, 2D materials were produced theoretically.[28]

Eventually, graphene was successfully produced in the laboratory using mechanical exfoliation by Scotch tape, and was used to fabricate field effect transistors.[29] The outstanding electrical and mechanical properties of 2D materials have accelerated its development. The lack of bandgap and half metallic behaviour of graphene, however, limited its usage in optoelectronics. 2D materials with bandgaps such as graphene oxide or transition metal dichalcogenides (TMDs) are used instead.

TMDs compounds consist of chalcogen elements (S, Se, Te) and group IV, V, VI transition metals. Like graphene, many TMDs possess a layered structure. The force between the adjacent layers in such materials is the weak van der Waals force. The transition metal and chalcogen atoms are bonded by strong covalent bonds within each layer. There are two types of crystal structures for layered TMDs, which are 1T and 2H phases (Fig1.2-1). 1T and 2H phases have octahedral

and trigonal structures respectively. TMDs based on group IV and VI elements tend to form 1T and 2H structures respectively, while Group V TMDs have similar energies in both structures. In terms of electrical conduction, TMDs can range from semi-conductors ($MoS_2$, $WS_2$), superconductors ($NbSe_2$) and semi-metals ($WTe_2$, $TiSe_2$), due to the *d*-orbital of transition metal. The energy level in the *d*-orbital is relatively narrow. The occupation of different energy levels in the *d*-orbital change the properties of TMDs.

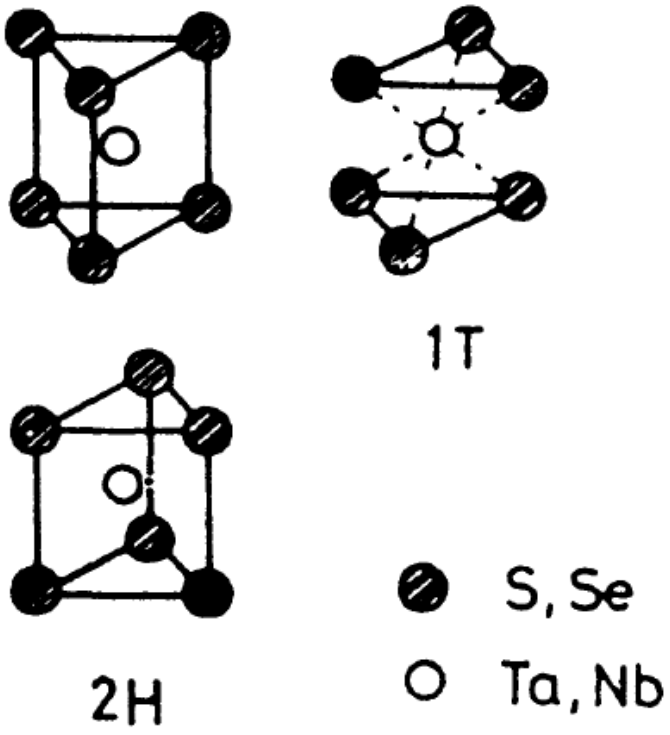


*Fig. 1.2-1 Octahedral and trigonal structures of TMDs layers[30].*

$MoS_2$ is one of the semi-conductor TMDs. The first monolayer $MoS_2$ was

prepared by mechanical exfoliation and transistors were fabricated from such monolayer flakes.[31] It was reported that the 2H-$MoS_2$ phase is more stable than 1T-$MoS_2$. 2H-$MoS_2$ is a semiconductor and 1T-$MoS_2$ is metallic.[32] In following, $MoS_2$ is taken as 2H-$MoS_2$, because of the instability and difficulty in producing 1T-$MoS_2$. The bond length between Mo and S in $MoS_2$ is 2.37Å, while the lattice constant is 3.11Å. [33] The outstanding mechanical behavior of $MoS_2$ shows its potential for flexible electronic devices,[34] as experimental results have shown that $MoS_2$ retained the electrical properties even under the bending with the radius of curvature down to 0.75 mm.[35]

The number of layers of TMDs strongly affects the electron states and the band diagram of such materials. For single layer TMDs such as $MoS_2$ or $WS_2$, the band structure shows a direct bandgap at the *K* point, but shows indirect bandgap in bulk form at *K* and $\Gamma$ points. The electronic state around $\Gamma$ point is related to the combination of *d* orbital of Mo and $p_z$ orbital of S, which is affected by interlayer interaction.[36] The layer dependence of bandstructure is also revealed in Raman spectroscopy. There are four Raman vibration modes of $MoS_2$ which are $E_{1g}$, $E^1_{2g}$, $A_{1g}$ and $E^2_{2g}$. The vibration direction of each mode is shown in Fig.

1.2-2. The $E^1_{2g}$ and $A_{1g}$ modes are shifted when the number of layers decreases. The $E^2_{2g}$ mode does not occur in monolayer $MoS_2$. Therefore, Raman spectroscopy is a simple method to find the number of layer of $MoS_2$ in the sample.

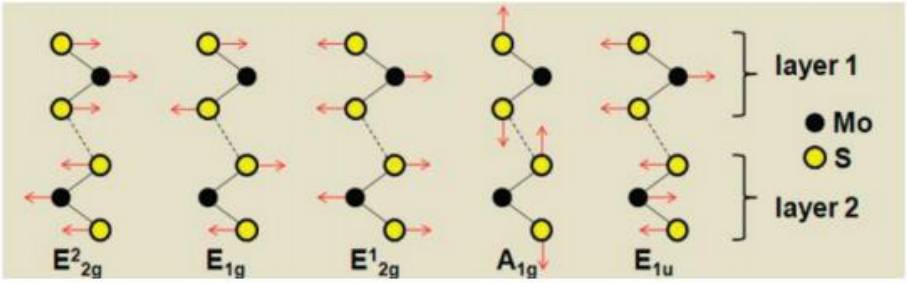


*Fig. 1.2-2 Schematic illustration of four Raman vibration modes [37].*

Considering the preparation of 2D materials, the first 2D material was produced by mechanical exfoliation from graphite crystals.[29] By using Scotch tape, 2D materials were exfoliated and then transferred on receiving substrates. This method can be used for producing various layered materials such as graphene [29], $MoS_2$ [31], boron nitride [38] and phosphorene [38]. The technique is suitable for research of new layered materials and related device heterostructures.[39-41] However, the monolayer flakes produced are small and the production yield is low.

Another type of exfoliation is chemical exfoliation. There are two types of chemical exfoliation, namely solvent-based exfoliation [42, 43] and ion

intercalation [44, 45]. Although both of them have a high yield of monolayer TMDs compared with mechanical exfoliation, the size of monolayer flakes are only up to a few microns.

Chemical vapour deposition (CVD) is a more promising method to grow large area $MoS_2$.[46, 47] It mainly uses a precursor which contains Mo and react under S or $H_2S$ environment. The limitation of the CVD method is the strong substrate dependence of yield and the high processing temperatures.

The last method of preparing 2D materials is the physical vapour deposition such as sputtering or pulsed laser deposition.[48-50] The large area and substrate independence of yield shows the potential of large area production of 2D materials by physical vapour deposition. However, the quality of $MoS_2$ formed is inferior as compared with those prepared by other methods mentioned.

## 1.3. Spintronics devices based on two dimensional materials

Research in spintronics of 2D materials started with graphene. Long spin life time (1-6 ns at 4 K) and long spin diffusion length (3-12 μm at 300 K) were reported in lateral spin valve devices based on graphene. [1, 2] Defects in

graphene were also suggested to induce magnetism.[51-53] These researches bring prospects for spin logic devices. [3]

The spin properties of $MoS_2$ is also outstanding. First-principle transport calculations showed a large magnetoresistance effect (near 300%) in Fe/$MoS_2$/Fe junctions. Fe atoms can strong hybridization with S atoms in the $MoS_2$ spacer layer, which increases the spin injection efficiency in such junctions.[5] However, the experiment results of $MoS_2$-based spin valve NiFe/$MoS_2$/NiFe showed only moderate MR of 0.7%.[6] The reported spin valve structure was fabricated using CVD-grown $MoS_2$ prepared by wet transfer method. The large difference of experiment and calculation results could be due to the production or processing method of $MoS_2$.

The spin related properties of $MoS_2$ have close interaction with the valley degree of freedom. Valleys in $MoS_2$ have a great dependence with the number of layers. Pervious literature showed a long hole valley-spin lifetime (>1 ns) in monolayer $MoS_2$, which is much reduced in bilayer $MoS_2$ (few hundred femtoseconds).[54] The inversion symmetry present in bilayer $MoS_2$ is broken in monolayer $MoS_2$, causing the coupling of spin and valley degrees of freedom. The

spin degeneracy near the valence band is split, causing intervalley transport to hole spin down state forbidden. This cause the long valley-spin lifetime for holes in monolayer $MoS_2$. Another literature reported calculation results on the spin-polarized electronic transport in monolayer $MoS_2$ devices using Monte Carlo method. The monolayer $MoS_2$ spin channel showed a long relaxation length of 0.4 μm at room temperature. [55]

The high spin life time and diffusion length of $MoS_2$ show its potential for spin valve devices. The high MR of $MoS_2$ vertical spin valve by calculation results give support to use $MoS_2$ as the spacer layer.

## 1.4. Structure of thesis

This thesis is arranged as shown in the following:

In this Chapter, a brief introduction and theory of two dimensional materials and spintronics was provided. The literature review shows the potential of $MoS_2$-based spintronic devices from experiment and calculation results.

In Chapter 2, the techniques needed to fabricate $MoS_2$ spin valve devices are introduced. The first section will give details on the deposition method, and

followed by the techniques for characterization of $MoS_2$, magnetic electrodes and the spin valve devices.

In Chapter 3, the production method of $MoS_2$ will be discussed. $MoS_2$ in this research were produced by chemical vapor deposition, mechanical exfoliation, and magnetron sputtering. The quality of $MoS_2$ was mainly characterized by Raman spectroscopy. The comparison between different $MoS_2$ production methods will be given.

In Chapter 4, the $MoS_2$ vertical spin valve were fabricated and characterized. The magnetic measurement and electric measurement results will be shown.

The last Chapter concludes the project and provide suggestion on potential future work concerning this research field.

# Chapter 2. **Experimental Techniques**

## 2.1. **Device fabrication**

In this section, the deposition techniques used in this project will be discussed. They are pulsed laser deposition, magnetron sputtering and e-beam evaporation. The detail methods to produce TMDs will be discussed in Chapter 3.

### 2.1.1. Pulsed laser deposition

Pulsed laser deposition (PLD) is a deposition method which uses a focused pulsed laser to vaporize the target material. It is a physical vapor deposition technique. PLD can be used for the growth of epitaxial films for various materials. PLD started to draw much attention after the preparation of high-$T_C$ superconductor films of Y-Ba-Cu-O(YBCO) in 1987. [56]

A PLD system generally consists of a vacuum chamber and a high-energy pulsed laser source. PLD can be performed under high vacuum with flowing gas. The substrates are generally heated up during the deposition, and are typically followed by a post annealing process to improve the film crystallinity. Inside the chamber, a target holder is placed on the path of the laser beam, and the substrate holder and the heater are positioned facing the target.

In the PLD process, the focused laser pulses strike on the target. The laser pulse will penetrate through the target surface, absorbing the laser energy. The depth of penetration is dependent on the complex refractive index and wavelength of the laser used. The high energy laser pulses excite the electrons of the target to become free electrons. The free electrons collide inside the target, vaporizing the target surface and creating a plasma plume. Then, the plasma plume expands because of Coulomb repulsion force. The shape of the plasma is a 3D Gaussian shape. The shape and size of the plume is dependent on the pressure inside the chamber. Increasing the chamber pressure causes a decrease of plume size and kinetic energy of the plasma. After that, the materials from the target are deposited on the substrate. If the kinetic energy of the plasma is too high, it will cause defects or vacancies on the films.[57] Finally, the deposition materials will nucleate and grow. There are three growth modes for PLD, namely step-flow growth, layer-by-layer growth and 3D growth. The growth mode adopted is dependent on the deposition parameters chosen.

PLD can be used for the deposition of a wide range of materials such as oxides, TMDs and metals. However, because of the size of the plume, the film

thickness can vary significantly on the surface of the substrates. There is only around 10 $mm^2$ of area on the substrates surrounding the center of the plume where uniform films can be obtained.

### 2.1.2. Magnetron sputtering deposition

Similar to PLD, magnetron sputtering deposition is a physical vapor deposition technique. Sputtering refers to the process that materials are ejected from target surfaces by the bombardment of high energy particles. Magnetron sputtering deposition generally uses ionized gas as the high-energy particle source. Gas molecules flowing into the magnetron sputtering chamber become ionized by the electric field applied between the target and the substrate. The ionized gas accelerates towards the target. To increase the yield rate of sputtering process, a magnetic field is typically applied by a permanent magnet behind the target. After the first gas atoms are ionized, the ions will be trapped by the magnetic field. The spiral movement will increase the bombardment chance at the target.

The applied electric field can be direct (DC) or alternating (AC) in nature, depending on the target materials. DC sputtering is used for the deposition of metals, while for insulating targets radio frequency (RF) AC field are needed.

There are several parameters that can affect the magnetron sputtering process. The type of gas affects the formation of films. If a reactive gas is flowing during sputtering, reaction will take place on the target particles before landing on the substrate; Ar is used as an inert gas to fill in the chamber. The gas pressure affects the number of ions that bombard on the target and the rate of target material ejection. However, a high gas pressure lowers the mean free path of materials ejected from the target and will affect the films' microstructure. The sputtering power is related to the deposition rate of materials.

### 2.1.3. Electron beam evaporation deposition (EBD)

Electron beam evaporation deposition (EBD) uses electron beam bombardment to evaporate target materials. EBD is a kind of physical vapor deposition. The mechanism behind EBD is similar to thermal evaporation. EBD have lower chance of impurity contamination compared to thermal evaporation, which mainly comes from thermal source such as tungsten wire during heating.

For the electron beam to travel from the electron gun to target materials, the chamber needs to achieve a pressure better than $10^{-2}$ Pa. The electron beam can be generated by thermionic emission or field emission. By using a magnetic

field, the beam trajectory can be changed to control the location of electron bombardment in the crucible. A water cooling system is in place under the crucible, in order to prevent the evaporation of contaminants.

EBD can deposit a wide range of materials such as metals or oxides with evaporation temperature under 3000ºC. However, target materials which can decompose at high temperatures cannot be deposited by EBD.

## 2.2. Device characterisation techniques

In this project, the quality and surface morphology study of $MoS_2$ were mainly performed using Raman spectroscopy and atomic force microscopy (AFM). The magnetic properties of the electrodes were measured by vibrating sample magnetometery (VSM). X-ray diffractometry (XRD) was used to characterize the crystal structure and the epitaxy of the films. Details about the electrical measurements will be disused in Chapter 5.

### 2.2.1. Raman spectroscopy

Raman spectroscopy is widely used in chemical or crystal lattice identification. It uses a laser to illuminate on the samples and measure the light of

Raman scattering. Recently, Raman spectroscopy has become a versatile method to characterize 2D materials.[58-60]

Raman spectroscopy measures the scattering spectrum of the samples under laser illumination. The spectrum consists of three types of scattering, Rayleigh scattering, Stokes and anti-Stokes Raman scattering. When a photon is incident on molecules or atoms, they will be excited to a virtual high-energy state. They will quickly return to another real energy state and emit a scattered photon. If the energy of the final state is the same as the initial state, it is called Rayleigh scattering. It is an elastic scattering, which means the energy of the incident photon is the same as the scattered photon. If the energy of the final state is higher or low than the initial state, it is called Stokes Raman scattering and anti-Stokes Raman scattering respectively. Both Raman scattering are inelastic scattering.

Raman spectroscopy uses a laser as the incident photon source. A grating or monochromator is used to acquire scattering spectrum from the sample. To filter the high intensity Rayleigh scattering, notch filter or step filter is needed and is inserted in front of the grating. Raman shift, which is used to represent the spectrum from Raman spectroscopy, is proportional to energy. Its unit is

wavenumber ($cm^{-1}$). The equation of Raman shift is shown in following:

$$Raman\ shift = \left(\frac{1}{\lambda_o} - \frac{1}{\lambda_1}\right)$$

Where $\lambda_o$ is the wavelength of the excitation source and $\lambda_1$ is the wavelength of scattering spectrum. The peaks in the Raman spectrum are related to the vibration modes of the sample.

The Raman spectrometer used in this research was HORIBA HR800 and the wavelength of the laser was 488 nm.

### 2.2.2. Atomic force microscopy (AFM)

Atomic force microscopy (AFM) is a kind of scanning probe microscopy (SPM). It can be used to obtain the surface morphology of samples, perform lithography or manipulate atoms. The spatial resolution of AFM is in the order of nanometers. The radius of the tip is around a few nanometers. The setup of AFM is shown in Fig. 2.2.2-1

The mechanism of AFM is based on the atomic force interaction between AFM probe tip and the surface of samples. The atomic force is proportional to the distance between the tip and the sample surface. In the AFM setup, a laser illuminates the back of the probe and the spot is reflected to a detector. Bending

or vibration of the probe caused by the atomic force leads to the shifting of the reflected laser spot from the tip is, which is probed by the detector. After analyzing the signals obtained from the detector, the data is fed to the AFM stage which controls the piezoelectric crystal to maintains the probe-sample separation. The change of the height corresponds to the surface morphology.

There are two modes of operation in AFM measurements, namely contact mode and non-contact mode (tapping mode). In the contact mode, the probe is forced to approach to the sample surface and the degree of probe bending is used to detect the surface morphology. Contact mode has the issue of easy damaging of the probes. The non-contact mode is based on the vibration frequency change of the probe. The probe holder generates an oscillating frequency which is the resonance frequency of the probe. The amplitude of oscillation decreases when it is close to the sample surface. The controller on the AFM maintains the oscillation amplitude of the probe. Non-contact mode has the probe operating at a longer distance from the sample and the tips can survive more scans. The AFM system used in this research is the Burker Nanoscope 8 scanning probe microscopy.

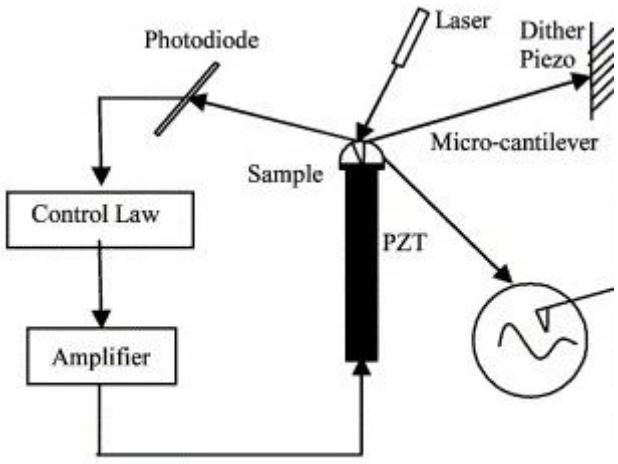


*Fig. 2.2.2-1 Graphical illustration of AFM setup. [61]*

### 2.2.3. X-ray diffractometry (XRD)

X-ray diffractometry (XRD) is used to study crystal structure and lattice parameters of the samples. When X-ray is incident on the crystal lattice, the scattering of X-ray in the lattice will cause destructive interference in most angles, and only in certain angles can constructive interference be obtained. These angles are given by the Bragg's law:

$$2d \sin\theta = n\lambda$$

where $d$ is the distance between the atomic planes, $\theta$ is the incident angle of the X-ray, $\lambda$ is the wavelength of the X-ray beam and $n$ is an integer. Different materials can result in different diffraction patterns and thus serve as the unique fingerprint of the material. This material fingerprint is collected in powder

diffraction files (PDF).

The schematic diagram of XRD is shown in Fig. 2.2.3-1. A XRD system consists of an X-ray source, sample holder and an x-ray detector. The X-ray is generated by a high-energy electron beam bombarding on a target material such as Cu, Mo, W or Cr. Different target materials create different characteristic X-ray emission lines. The two most high intensity X-ray lines are called $K_\alpha$ and $K_\beta$. Typically only $K_\alpha$ is used in XRD and therefore $K_\beta$ filter is inserted before the X-ray source to absorb the $K_\beta$ line for a monochromatic source. The X-ray detector and sample holder can scan about different axes to obtain different types of scan profiles and information about the sample crystallinity.

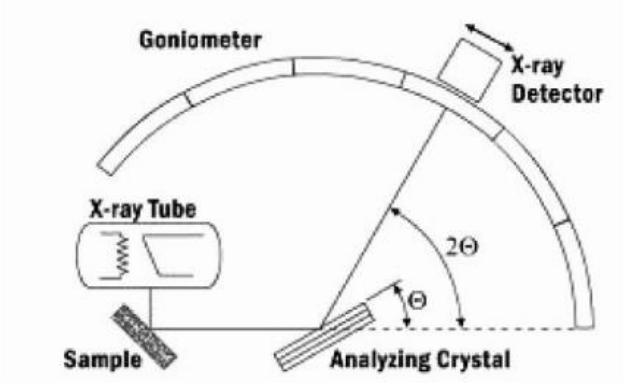


*Fig. 2.2.3-1 Schematic diagram of XRD.[62]*

This project used a SmartLab XRD system with Cu $K_\alpha$ source for X-ray. The wavelength of the $K_\alpha$ line of Cu is 0.154 nm.

### 2.2.4. Vibrating sample magnetometer (VSM)

Vibrating sample magnetometer is used to measure the magnetic properties of the samples. Sample to be measured is mounted on a probe and is vibrated in the magnetic field. Magnetization of the vibrating sample causes a changing magnetic flux through the pickup coils and an electromotive force (e.m.f.) is induced. The e.m.f. signal is amplified using a lock-in amplifier. A reference sample is needed to calibrate the relation between magnetization and the induced e.m.f. The schematic diagram of the VSM is shown in Fig. 2.2.4-1.

The VSM used in this project is Lakeshore 7800 for room temperature measurements, and Quantum Design model 6000 for low temperature measurements. The Quantum Design instrument can measure in the temperature range of 2 K-290 K, with a superconductor magnet that can give magnetic field up to 9 T.

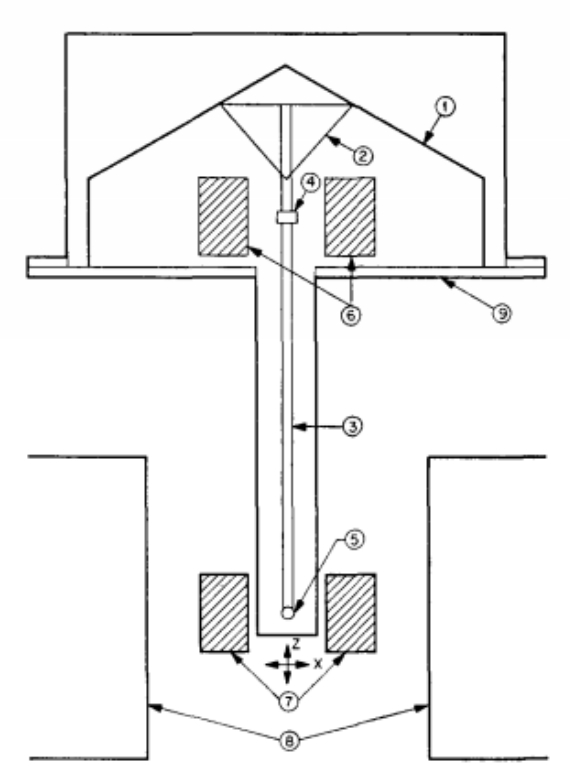


*Fig. 2.2.4-1 Schematic diagram of VSM 1. Vibration generator 2.suppot of the sample rod 3.sample rod 4.reference sample 5.sample 6.referance coil 7.sample coils 8.electromagnet.[63]*

# Chapter 3. Electrical contacts between electrodes and TMDs

## 3.1. Fabrication of TMDs on electrodes

In this project, vertical spin valves with TMDs as the spacer layer were fabricated. The detailed device structure will be discussed in Chapter 4. Because of the structure of the spin valve, TMD has to be produced on top of the bottom electrodes. Two methods were attempted to achieve this aim. The first method is the transfer method, which use TMDs flakes prepared by mechanical exfoliation or CVD and transfer them onto the electrodes. The transfer method can be categorized into two types, namely dry transfer and wet transfer. The other method is the direct deposition of TMDs on the electrodes. The deposition methods used in this project were RF magnetron sputtering and CVD. Raman spectroscopy were used to determine the number of layers and crystallinity of the TMDs produced. AFM measurements were used to confirm the thickness and morphology of the TMDs.

### 3.1.1. TMD transfer process

Transfer of CVD 2D materials to different substrates were performed for

devices fabrication in the early stage of this project. This kind of transfer was achieved by coating the poly(methyl methacrylate) (PMMA) to protect and support the TMD flakes. The PMMA/TMD is then released by etching the Si substrate, followed by a fishing process using the target substrate.

The fabrication of devices based on exfoliated 2D materials relies on the e-beam lithography (EBL) to draw electrode patterns, followed by a lift off process to prepare the electrodes on the top of the flakes. Because of the sandwich device structure, the 2D materials need to be precisely placed on the bottom electrode. Therefore, the device cannot be fabricated by using only the EBL.

During the transfer process, $MoS_2$ flakes attached on PMMA membrane have to be manipulated on the bottom electrode track. Therefore, PDMS transfer method was used.[64] This method relies on the viscoelastic properties of PDMS. For transferring exfoliated TMD, the PDMS was put on the flakes. Then, the PDMS was quickly peeled off, and the viscoelastic behavior of PDMS allowed the TMD to adhere on the PDMS under fast peeling. By using a glass slide to pick up the PDMS, the glass slide with the PDMS block was placed on the micro XYZ stage under the microscope. By manipulating TMDs on the target electrode and

slowly peeling off the PDMS, the TMD was released on the electrode. For CVD-grown TMD attached to PMMA, the PMMA membrane was fished by the PDMS block and released dissolving the PMMA in acetone. The setup of PDMS transfer method is shown in Fig. 3.1.1-1. In contrast with most of the transfer methods which involve organic solvent or etchant solutions, PDMS-based transfer can be performed solvent-free.


*Fig. 3.1.1-1 PDMS transfer method setup*

The yield rate of mechanically released PDMS is not high. Successful pick up and release of TMD is influenced by many factors such as the roughness of sample electrodes, and the cleanness of the substrates on which the TMDs are

grown. To increase the yield rate of manipulation, multiple polymer layers (polyvinyl acetate(PVA)/PMMA) was spin-coated on the substrate before exfoliation. Because of the different solvents used for PMMA and PVA, after the exfoliation process by the polymers, the sample were put in the water for dissolving the PVA layer and releasing the PMMA/TMDS membrane. A fishing processing with PDMS was followed, allowing it to be in contact with the PMMA. After the manipulation, PMMA layer could be dissolved by acetone to release the TMD on electrodes.

Fig. 3.1.1-2 is shows the transfer process. A $MoS_2$ sample was fabricated by mechanical exfoliation from a $MoS_2$ single crystal by the Scotch tape method. It was exfoliated on Si substrate with pre-coated polymer multilayer. The 5% PVA in water was spin-coated at 4000 revolutions per minutes (rpm) on the Si substrate, followed by a post-baking process at 120°C for 10 min. The 5% PMMA solute in acetone was spin-coated at 5000 rpm. The post-baking condition was 100°C for 5 min.

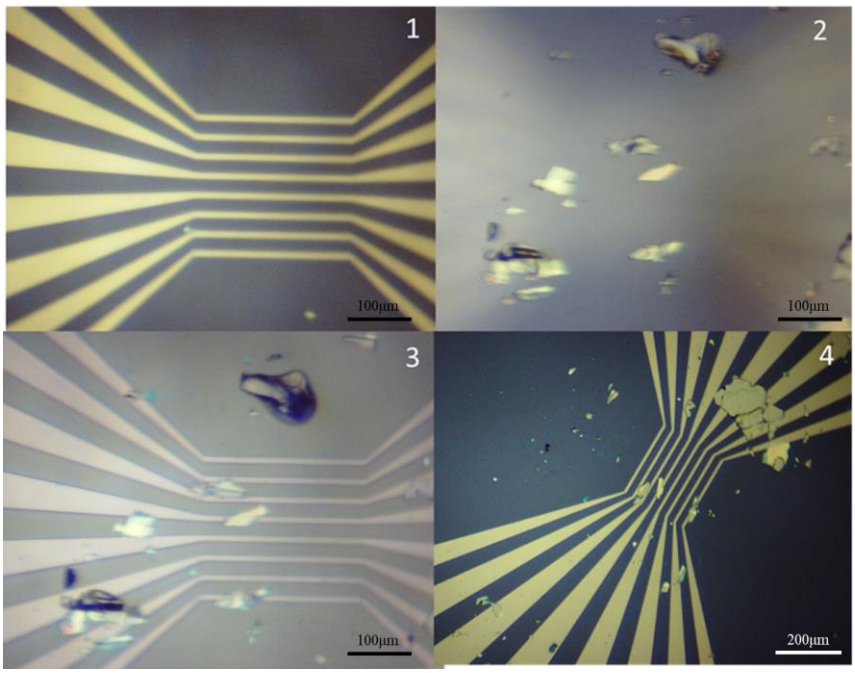


*Fig. 3.1.1-2 Microscope images of the PDMS/PVA/PMMS transfer process: (1) bottom electrode pattern; (2) exfoliated $MoS_2$ on PMMA/PDMS; (3) after the alignment process, the $MoS_2$ was manipulated on bottom electrode; (4) after dissolving the PMMA and releasing the $MoS_2$ on the bottom electrode.*

Similar method was used to manipulate CVD $MoS_2$ flakes. CVD $MoS_2$ samples were grown on the Si substrates. PMMA was spin-coated at 4000 rpm on the $MoS_2$ for protection, followed by baking at 120°C for 2 min. Then, the sample was put in the 0.5 M NaOH solution to peel off the $MoS_2$/PMMA membrane; the peel off process was done within 2 min to prevent the damage of $MoS_2$ by NaOH solution. The fishing and sample manipulating processes are identical to previous descriptions. Fig. 3.1.1-3 shows the microscope images of CVD $MoS_2$ on Si and PDMS.

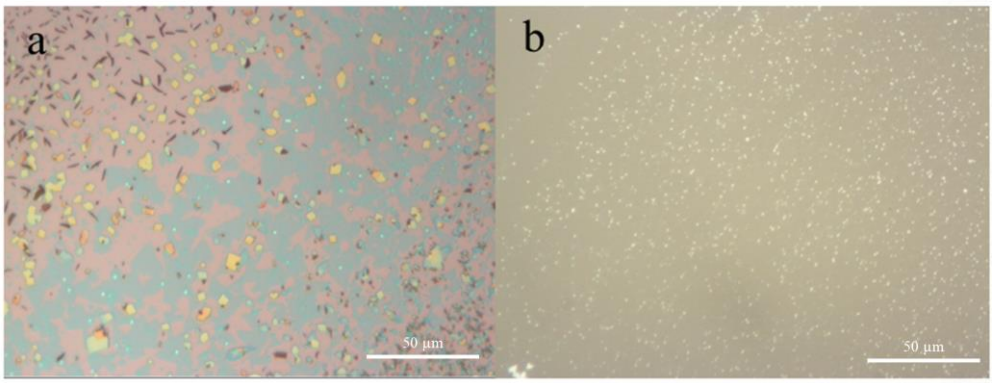


*Fig. 3.1.1-3 Microscope images of (a) CVD $MoS_2$ on Si (b) CVD $MoS_2$ on PDMS after fishing. Scale bar = 50 µm.*

### 3.1.2. Direct deposition of TMD

Direct deposition of TMD on bottom electrodes is a much easier way to prepare the materials as compared with the transfer method. The common method of depositing TMD on substrates are CVD or sulphurization from metal films. In this project, the TMD needs to be grown on the electrodes, and most metal electrodes react with the precursors during the high temperature CVD process. Most of the recent researches focus on the growth of TMDs on Si or sapphire substrates. [65, 66] In this project, CVD and RF magnetron sputtering were used to produce TMD on $La_{0.7}Sr_{0.3}MnO_3$ (LSMO) electrodes. LSMO is a ferromagnetic oxide which is deposited under 700°C, and should be stable under CVD process. Before the CVD process, the stability of LSMO under CVD process has to be

confirmed.

VSM measurements of LSMO films were performed before and after the CVD to confirm the stability of LSMO. Fig. 3.1.2-1 shows the MH loops before and after the CVD process in sulphur vapour at 750°C. The result shows that the coercive field of LSMO film remains the same. On the other hand, the saturation magnetization of the MH loop become flat after the process. This phenomenon is caused by the expansion of grain size after the CVD process. The result suggests that the LSMO can retain its magnetic properties during the CVD or sulphurization process.

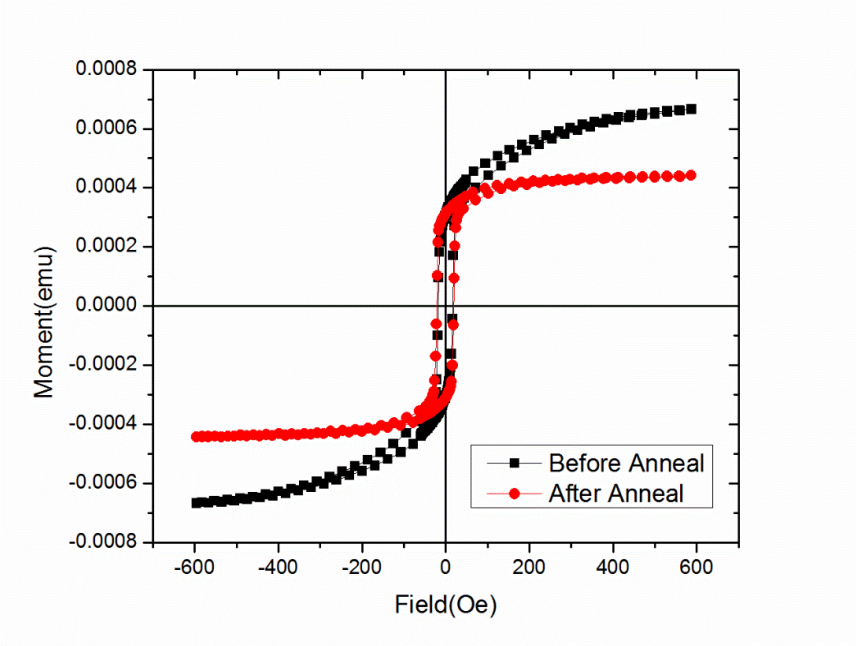


*Fig. 3.1.2-1 MH loop of LSMO film before (black) and after (red) annealing in sulphur vapour.*

The CVD $MoS_2$ on LSMO was performed afterward. The same condition which was used to CVD $MoS_2$ on Si and sapphire, however, did not support the $MoS_2$ growth on LSMO. None of the $MoS_2$ signature Raman peak was obtained on CVD $MoS_2$ on LSMO sample. It may due to the surface potential and surface roughness difference between LSMO and Si. Chemical processes are highly sensitive to those parameters. Eventually, CVD was not adopted for this project.

As CVD cannot be used to grow TMD directly on magnetic electrodes, the simple way to prepare TMD is by physical deposition from the parent materials. RF sputtering has been used to produce $MoS_2$ on PDMS with $MoS_2$ target. [48] In the literature, laser was used to anneal the $MoS_2$ films after deposition to increase the crystallinity. I performed RF sputtering at room temperature at 6 mTorr Ar, following by an annealing process using the rapid thermal processing (RTP). Details of this process are discussed in the following section.

## 3.2. Characteristics of TMDs on electrodes

Raman spectroscopy is an easy way to measure the crystallinity and the

number of layers in TMD or 2D materials. The Raman peaks are related to the number of layers of $MoS_2$. The $E_{2g}$ and $A_{1g}$ peak positions are strongly influenced by the number of layers $n$ (when $n < 5$). The increasing transition energy at $K$ point, caused by the quantum confinement or elongated intralayer bonding, weakens the $A_{1g}$ phonon and leads to a peak shift,[67] which is a useful indicator for the thickness of ultra-thin $MoS_2$.

Exfoliated $MoS_2$ on PDMS/PMMA was measured by Raman spectroscopy with a 488-nm laser source. The Raman spectrum on this sample is shown in Fig. 3.2-1. Two positions on the sample were measured (black circle and red circle, left panel). The measured Raman peak intensity is smaller for the thin sample (red circle). The peak position of thick sample (black curve) and thin sample (red curve) are ($E_{2g}$ = 383 $cm^{-1}$, $A_{1g}$ = 408 $cm^{-1}$) and ($E_{2g}$ = 383.2 $cm^{-1}$, $A_{1g}$ = 404.8 $cm^{-1}$), respectively. The corresponding peak separations are 25 $cm^{-1}$ (thick sample) and 21.6 $cm^{-1}$ (thin sample). Comparing the data with previous literature,[67] the thin sample correspond to a bilayer sample and the thick sample has more than 4 layers. The result demonstrates the effect of number of layers on the Raman shift.

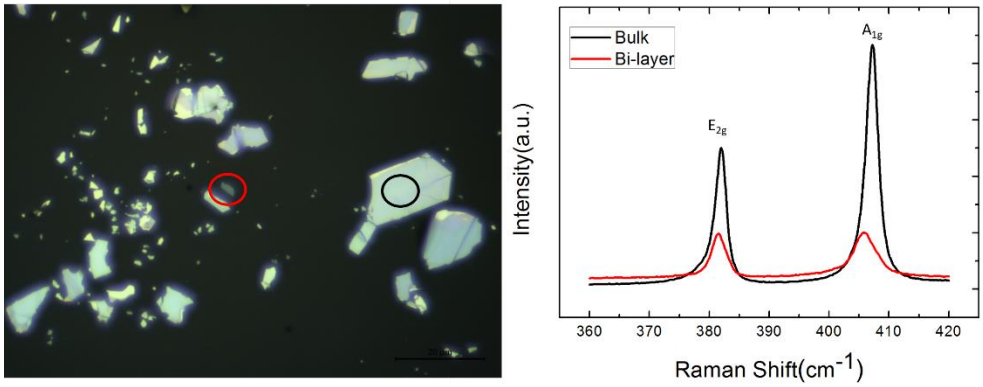


*Fig. 3.2-1 Raman spectroscopy of exfoliated $MoS_2$ on PDMS/PMMA. The black and red circles are the measured position which result in the black and red Raman spectra, respectively.*

The Raman spectrum of CVD $MoS_2$ on PDMS was also measured, and the results are shown in Fig. 3.2-2. This Raman spectrum was measured on the sample shown in Fig. 3.1.1-3. $E_{2g}$ and $A_{1g}$ peaks are located at 384.8 cm$^{-1}$ and 402.9 cm$^{-1}$ respectively. The peak separation of 18.1 cm$^{-1}$ implies that it is a monolayer $MoS_2$. The board peak at 480 cm$^{-1}$ is the Raman peak of PDMS. The result shows the successful transfer of CVD $MoS_2$ on PDMS. The sample is ready to be transferred onto electrodes.

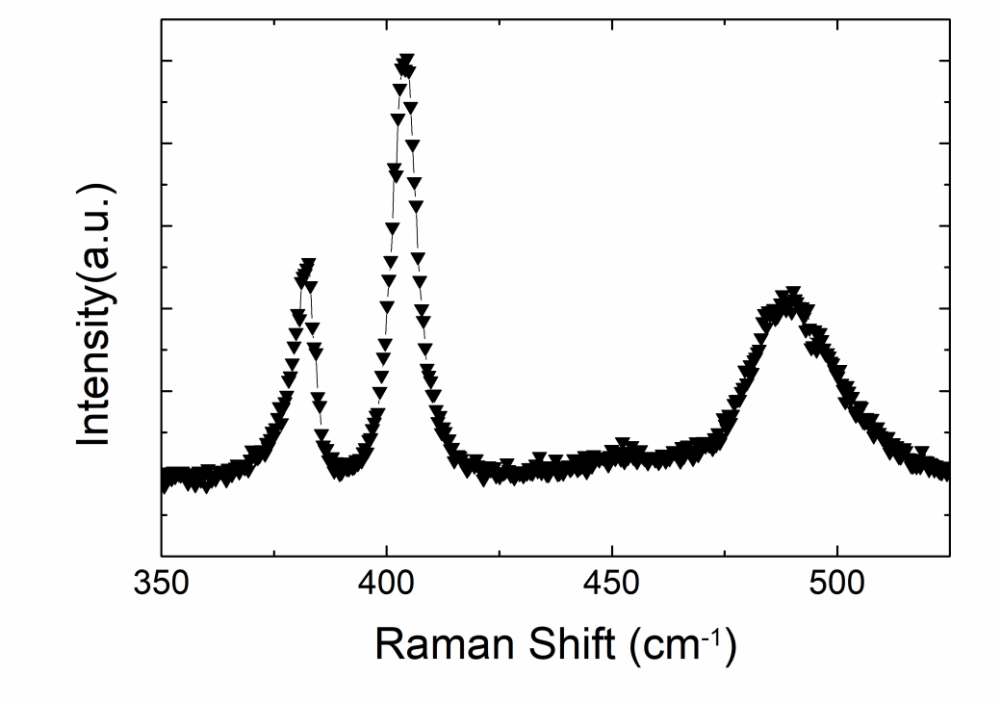


*Fig. 3.2-2 Raman spectrum from CVD $MoS_2$ on PDMS.*

After the sample was transferred onto the electrode surface, Raman mapping measurement was performed. Fig 3.2-3 shows the results of 1D Raman mapping and the microscope image of the $MoS_2$ transferred on the electrode. Both of the $MoS_2$ peaks can be obtained on the electrode. The peak at 520 $cm^{-1}$ is the Si substrate peak. The mapping data show a bathtub shape in all three peaks scanning across electrode. The lower intensity of Si peak is due to the blocking by the bottom electrode. However, for $MoS_2$ is on the electrode, the intensity drop could be due to the weak adhesion between the electrode and the $MoS_2$ an compared to $MoS_2$ on the flat substrate, which hinted that the $MoS_2$ on the

electrode may not be continuous.

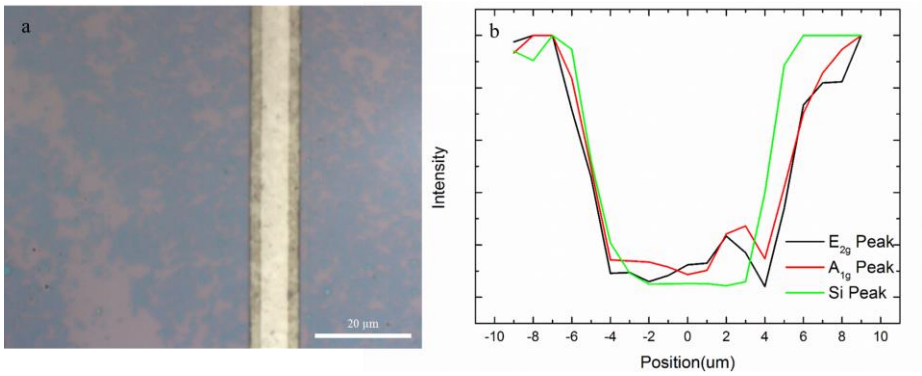


*Fig. 3.2-3 (a) Microscope image of CVD $MoS_2$ transferred on electrode. (b) Intensity mapping data for Si, $E_{2g}$ and $A_{1g}$ peaks across the electrode.*

The unsuccessful transfer and the low yield rate for transfer $MoS_2$ means that direct deposition (sputtering) of $MoS_2$ has to be used for this project. Sputtering of $MoS_2$ films was performed at room temperature and followed by post-annealing at 450°C *ex situ*. The need of post annealing and room temperature sputtering can be explained by the result of Raman spectroscopy (Fig3.2-4). Three samples were measured. The first one was deposited at room temperature for 3 minutes. The second one was deposited at room temperature for 90 s. The third one was deposit at 500°C for 30 minutes. All the three samples were treated with identical post-annealing process. The result shows that there is no difference for the 500°C deposited sample before and after post-annealing. On the other hand, room temperature-deposited sample shows a sharp change in Raman intensity due

to the annealing process. Moreover, the Raman intensity of the 500°C-deposited sample is much smaller that the room temperature-deposited sample, even it is deposited with twice the thickness.

The large difference of Raman spectra between the RT-deposited sample before and after post-annealing is due to the crystallization of $MoS_2$ film. RT deposition resulted in amorphous $MoS_2$ films. The post annealing process helped to improve the sample crystallinity. For the high temperature-sputtered sample, the Raman peak shows a small intensity and no change due to the post annealing process. The high temperature deposition resulted in the vaporization of sulphur from the sample, due to the low vapour pressure of sulphur in $MoS_2$. The resultant films were deficient in sulphur. Also since the sample was deposited at high temperature, the crystallization would have already taken place during the deposition process.

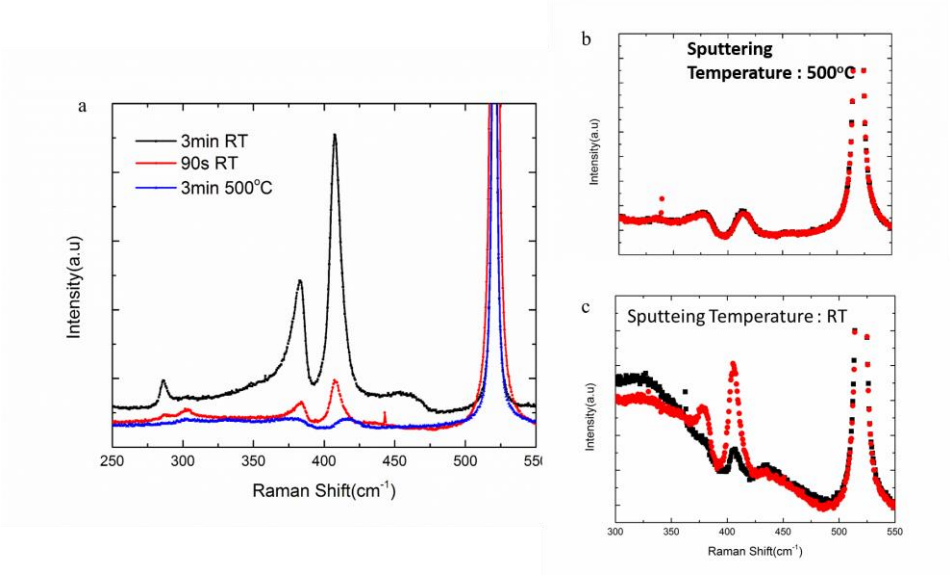


*Fig. 3.2-4 Raman spectra of $MoS_2$ film deposited and annealed at different conditions. (a)All three sample after post annealing; (b) high temperature-deposited sample before and after post-annealing; and (c) room temperature deposited sample before and after post-annealing.*

# Chapter 4.**Magnetoresistance of TMDs spin valves**

## 4.1. **Device fabrication**

TMD-based vertical spin valve devices were fabricated in this project. The device is a pseudo spin-valve with two different magnetic materials as free and hard layers. Four point measurements were used to characterise the devices.

### 4.1.1. Device structure

The spin valve device structure is shown in Fig. 4.1.1-1. A spin valve consists of two ferromagnetic layers (top and bottom electrodes) sandwiching a non-magnetic spacer layer of two-dimensional metal dichalcogenides ($2DMX_2$). The standard photolithography is followed by a lift off process; alternatively, shadow mask technique could be used to fabricate the patterned bottom and top electrodes. The ferromagnetic materials used were $La_{0.7}Sr_{0.3}MnO_3$ (LSMO), NiFe and Co. Pulsed laser deposition was used to deposit LSMO, and magnetron sputtering was used to deposit ferromagnetic metal bottom electrodes. The devices with the MoS2 prepared by transfer method used NiFe for bottom electrode. The bottom electrode width of device which were fabricated by transfer

method need to smaller than $MoS_2$ flakes. Therefore, metal electrode was chosen because of the ease to prepare narrow electrodes by lift off. The devices with sputtered $MoS_2$ have employed LSMO as bottom electrode. As the $MoS_2$ deposition process involved annealing at high temperature, LSMO bottom electrode was used as it is stable under the annealing process.

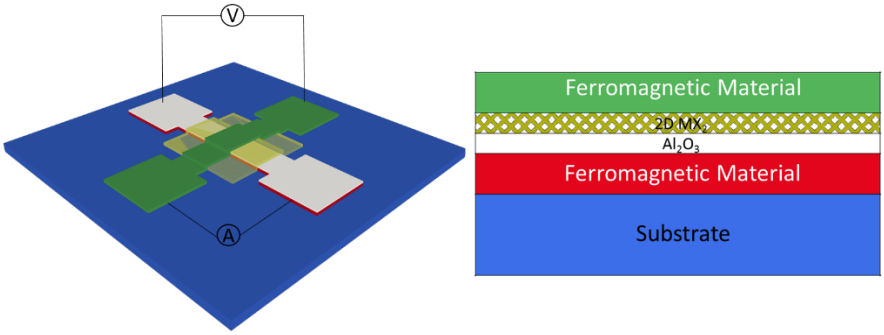


*Fig. 4.1.1-1 Device structure of TMD-based spin valve structure.*

Aluminum oxide was used as the insulator layer to increase the spin injection efficiency. Aluminum film was first deposited on top of the ferromagnetic metal *in situ* during the sputtering process, followed by an oxidation process to form the aluminum oxide spacer layer. Adding a spacer layer between the electrode and TMD was suggested as a means to increase the spin-injection efficiency into the TMD.[68] Table 4.1.1-1 showss the different contacts of graphene spintronic devices in literature;[68-70] the spin-injection efficiency

was calculated by the results of the magnetoresistance signals. The graphene spintronic device with direct contact on the ferromagnetic electrode showed a low MR and low spin-injection efficiency (< 1%). Continuous thin barriers between graphene and ferromagnetic material showed high MR and high spin-injection efficiency (> 60%). The low spin injection efficiency is the result of conductance mismatch between the layers. After adding the insulating thin barriers, the electron can tunnel through the insulating layer and the spin injection will be increased. Similar argument can also be applied to TMDs.

Table 4.1.1-1 Spin injection efficiency in different contacts.

| | **Transparent contacts [69]** | **Pinhole barriers [70]** | **Tunneling contacts [68]** |
|---|---|---|---|
| **Contact with FM electrode** | direct contact with graphene | barriers with pinhole between graphene and FM | continuous thin barriers between graphene and FM |
| **Non-local MR** | ~100 mΩ | ~10 Ω | ~130 Ω |
| **Spin-injection efficiency** | ~1 % | ~2-18 % | >60 % |

### 4.1.2. Film fabrication process

STO was used as the substrate for depositing LSMO. Before the deposition, STO substrates were treated to get an atomically flat and single terminated surface.

The substrates were annealed at 1000ºC for 3 hours, following by 1-minute dipping at 100ºC deionized-water bath. The whole process was then repeated once for further improvement of the surface quality; more repeats would not lead to any more significant improvement. [71] The AFM measurement shown in Fig. 4.1.2-1 shows step-terraces of step height 3.9Å, which is consistent with the (100) step height of STO substrates.

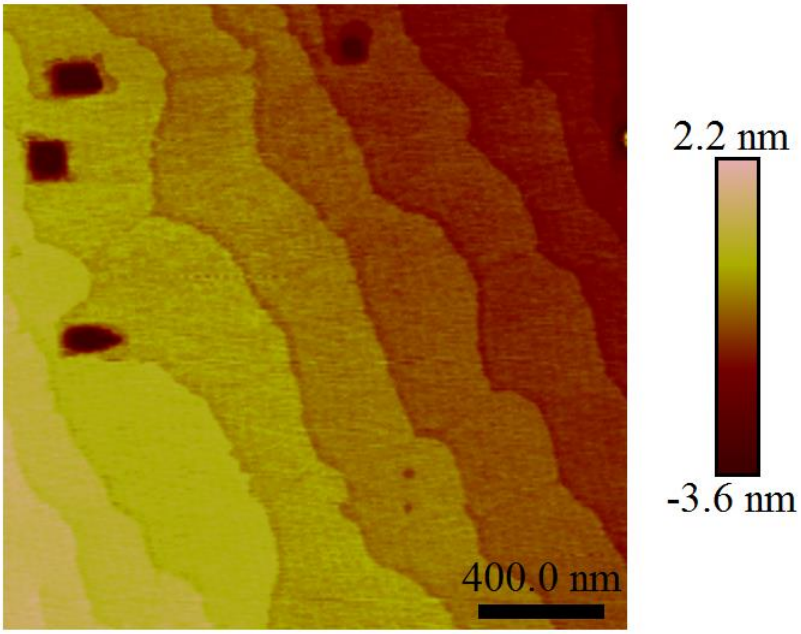


*Fig. 4.1.2-1 AFM image of deionized-water treatment STO(100) substrate.*

The LSMO layer was deposited on pre-treatment STO(100) substrates by PLD. The KrF (248 nm) laser was operated at 5 Hz with a pulse energy of 220 mJ. Films were deposited with an oxygen pressure of 120 mTorr at 700°C, followed

by a post-annealing process under 10 Torr oxygen pressure at 650°C for 10 min. The XRD scans of the LSMO film deposited is shown in Fig. 4.1.2-2. The XRD shows STO(002) and LSMO(002) peaks in *θ-2θ* scan. The full-wide at half-maximum (FWHM) of the LSMO(002) peak is 0.35°. The thickness of the film (20 nm) was confirmed by X-ray reflectivity (XRR) measurement. The XRD results suggest that high crystallinity LSMO was deposited.

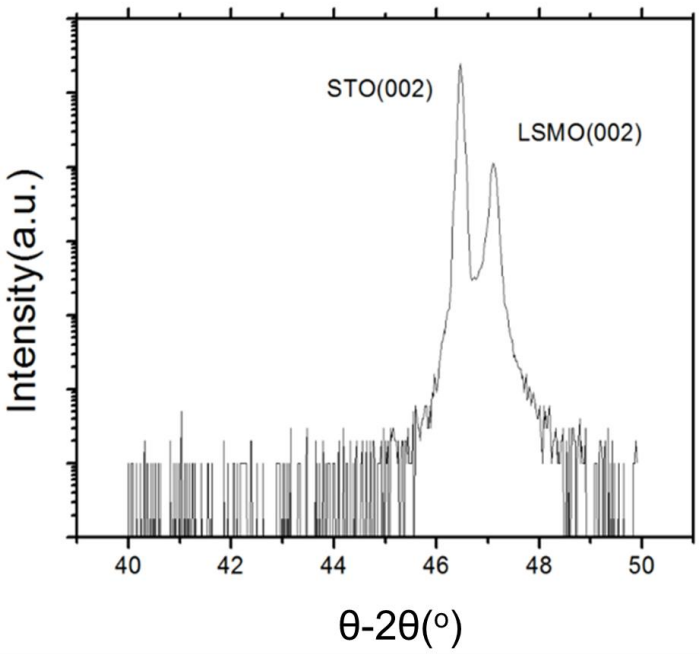


*Fig. 4.1.2-2 XRD of LSMO film on STO (001) substrate.*

Temperature-dependent resistance (*R-T*) measurement provides an indirect means to determine the Curie temperature ($T_C$) of LSMO.[72] At $T_C$, the

slope of the *R-T* curve changes from positive to negative. The *R-T* measurement from 20 K to 320 K is shown in Fig. 4.1.2-3. The slope remains positive at 320 K, which indicates the $T_C$ of LSMO is above the room temperature.

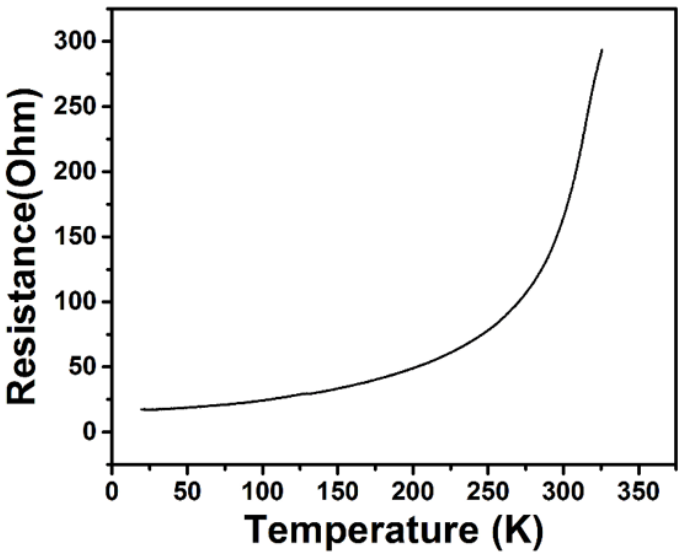


*Fig. 4.1.2-3 R-T measurement of LSMO thin film between 20-320 K*

## 4.2. **Magnetic property measurement**

As mention in Chapter 3, spin valves with exfoliated $MoS_2$ were fabricated by the dry transfer process. The device structure is NiFe (10 nm)/ $MoS_2$/Co (10 nm) on Si. Fig. 4.2-1(a) shows the microscope image of the dry-transferred $MoS_2$ spin valve device. The vertical electrode strip is 10 nm NiFe which was deposited

by sputtering, and the horizontal electrode is the 10 nm Co deposited by e-beam lithography (in order to prevent the damage of $MoS_2$ by high energy plasma). The junction area is 10×10 $\mu m^2$. Both top and bottom electrodes were patterned by photolithography and followed by a lift-off process.

The MR measurement (Fig 4.2-1c,d) was performed with the magnetic field in the sample plane. The MR signal can be seen to flip upside down when the direction of applied magnetic field changes. This indicate the measured MR is not due to spin valve effect through the junction but anisotropic magnetoresistance, because the MR signal is flipped when the magnetic field angle changes. This can be due to the contact of the bottom and top electrodes at the edges. The reason of the side contact is that $MoS_2$ cannot cover the whole bottom electrode.

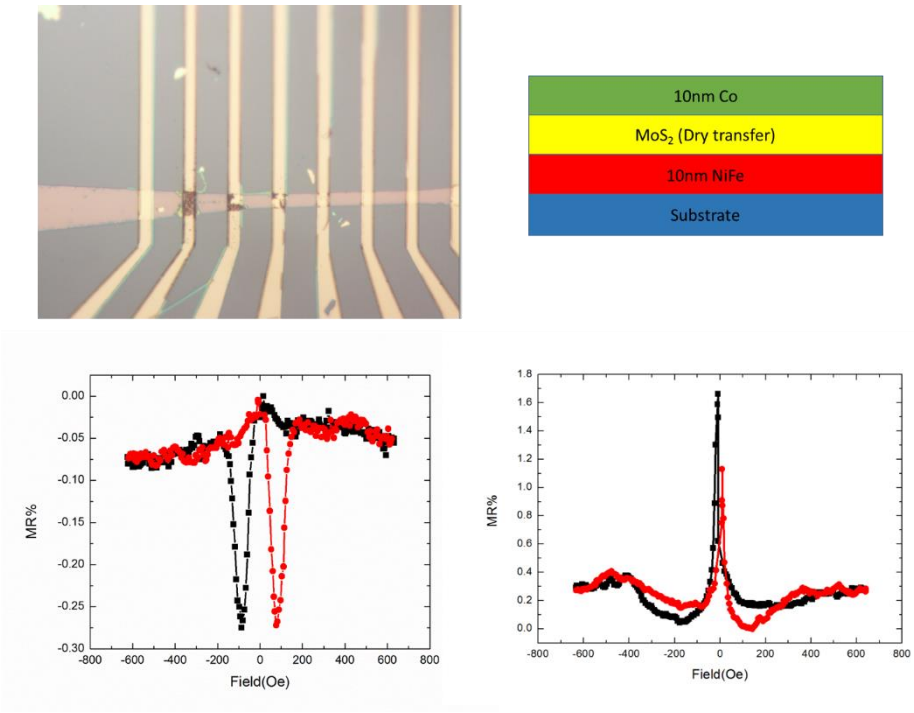


*Fig. 4.2-1 (a)Microscope image of dry-transferred spin valve junction. (b)Schematic of the junction. (c) and (d) show the MR measurement parallel and perpendicular to the bottom electrodes in the substrate plane, respectively.*

To prevent the side contact between the bottom and top electrodes, EBL process was deployed before the deposition of top electrode to define the contact of top electrode on $MoS_2$. The bottom electrode deposition and $MoS_2$ transfer method are identical as in the previous sample. After the $MoS_2$ transfer, PMMA layer was spin-coated on the sample (Fig. 4.2-2). A small hole was then created on PMMA by EBL above the bottom electrode and 2D materials. Then the top electrode was deposit on it. This method can prevent the side contact of electrodes and reduce the junction size.

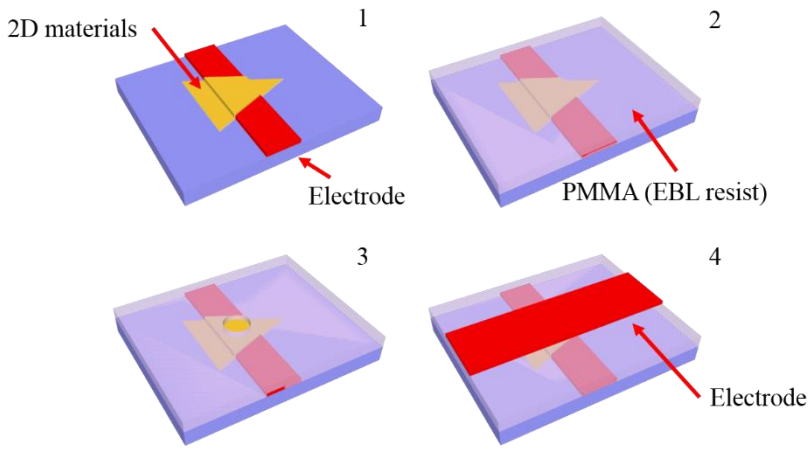


*Fig. 4.2-2 Schematic of device fabrication to prevent side contact.*

A control device (Si/NiFe (10 nm)/$AlO_x$ (2 nm)/Co (5 nm)/Au (80 nm)/ Ti (10 nm)) was fabricated using this method (Fig. 4.3-3(a)). Fig. 4.3-3(b) shows the microscope image of the sample which the junction radius of 1 μm. The four-point MR measurement was performed and the MR ratio is 0.07%.

To confirm the MR measured is not AMR, Fig. 4.3-3(d) shows the MR of the bottom electrode. The peak in the MR is different for the junction and the electrode. The $MoS_2$ spacer sample fabricated by this method showed small MR (MR% = 0.03%) in Fig4.3-3(c). It is speculated that interfacial contamination of the junction during transfer process contributed to the minute MR effect.

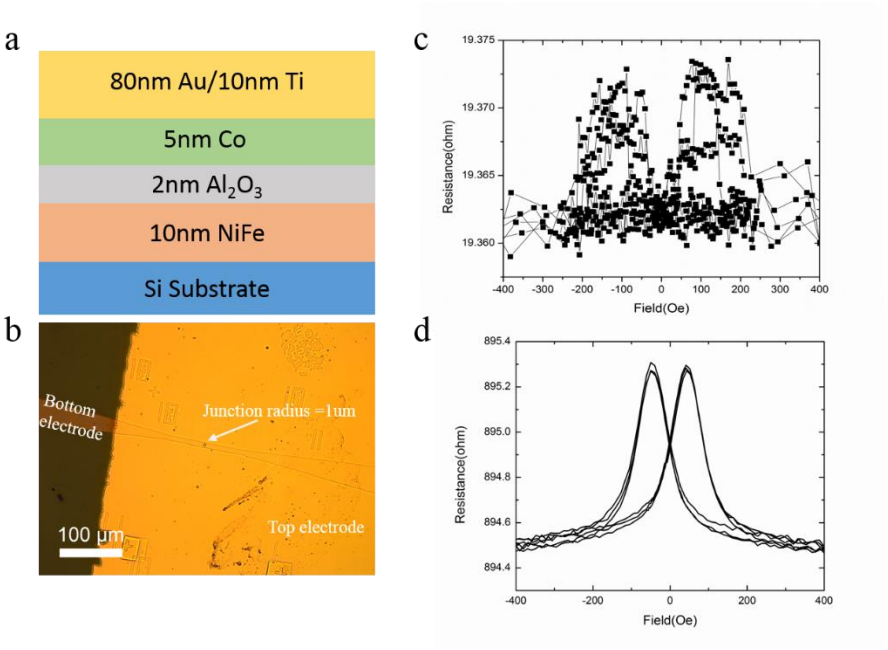


*Fig. 4.3-3 (a) Structure spin valve control sample. (b) Microscope image of control sample. (c) MR of device with CVD $MoS_2$ spacer. (d) MR of bottom electrode only.*

CVD preparation of $MoS_2$ is highly dependent on the substrate. $MoS_2$ cannot be grown directly on the magnetic electrode by CVD. Therefore, RF magnetron sputtering method was used to produce $MoS_2$ spacer. The deposition process and characterization of $MoS_2$ film was shown in Chapter 3. By using sputtering deposition, the thickness of $MoS_2$ film can be down to 2 nm. The Raman spectrum of 2 nm $MoS_2$ on Si (Fig. 4.3-4(a)) shows the signature peak of $MoS_2$. Using the optimized conditions for $MoS_2$ growth on Si substrates (room-temperature deposition followed by post-annealing in nitrogen), $MoS_2$ spacer was

prepared on LSMO and the Raman spectrum of LSMO/$MoS_2$ (Fig. 4.3-4(b)) shows the signature $E_{2g}$ and $A_{1g}$ peaks. This result shows that crystalline $MoS_2$ was deposited on STO/LSMO. The deposited $MoS_2$ on LSMO shows a high level of smoothness (Fig. 4.3-4(c), with root-mean-squared roughness = 0.31 nm). The NiFe/Au top electrode was finally deposited on top of $MoS_2$ by E-beam evaporation. A STO/LSMO (20 nm)/$MoS_2$ (2 nm)/NiFe (5 nm)/Au (50 nm) spin valve device was fabricated.

The deposition of LSMO was shown in the previous section. The MH loop of the complete spin valve sample (Fig. 4.3-4(d)) shows double coercivity at 18 Oe and 33 Oe at 20 K, which correspond to the coercivities of LSMO and NiFe, respectively. The double coercivity suggest the $MoS_2$ spacer magnetically decouples the LSMO and NiFe layers.

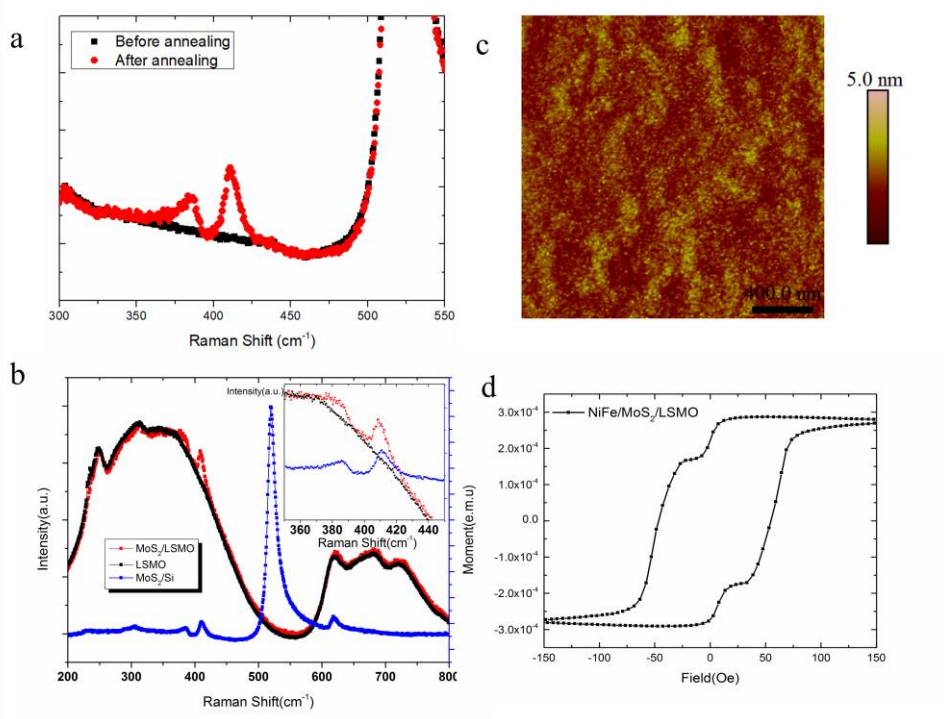


*Fig. 4.3-4 (a) Raman spectra of 2 nm $MoS_2$ on Si before (black) and after post-annealing (b) Raman spectra of 2 nm $MoS_2$ on STO/LSMO (red) and Si (blue). Black trace shows the spectrum of STO/LSMO. The board peak from 200 to ~ 450 $cm^{-1}$ is the peak of STO substrate. Inset highlights the data between 350 and 450 $cm^{-1}$. (c) AFM micrograph of the LSMO/$MoS_2$ after post annealing process. (d)Mh loop of STO/LSMO (20 nm)/$MoS_2$ (2 nm)/NiFe (5 nm)/Au (50 nm) spin valve device.*

Magnetoresistance (MR) measurement of the STO/LSMO (20 nm)/$MoS_2$ (2 nm)/NiFe (5 nm)/Au (50 nm) spin valve device was performed at 20 K. At this temperature, the zero-field resistance of the device was around 330 Ω as measured by four-point measurement. The MR result is shown in Fig. 4.3-5. A negative MR signal was obtained, which is similar to the result of LSMO/$BaTiO_3$(BTO)/NiFe

with no polarization of BTO.[73] The MR ratio of the device at 20 K is 0.8%. The switching field in MR curve matches with the double coercivity from MH loop in Fig. 4.3-4(d), which indicates the MR signal is due to the spin valve junction. To rule out the possibility of AMR from the magnetic electrodes, measurements were repeated by rotating the in-plane magnetic field through 90° (inset of Fig. 4.3-5(a)); the same negative MR behavior was measured. The result confirms that the MR obtained was due to the spin valve effect of the device. The IV measurement showed non-linear behaviour, which indicates the contact is not metallic (Fig. 4.3-5(b)). The low MR ratio may due to the sputtered $MoS_2$ is not single crystal but polycrystalline which limited the spin transfer.

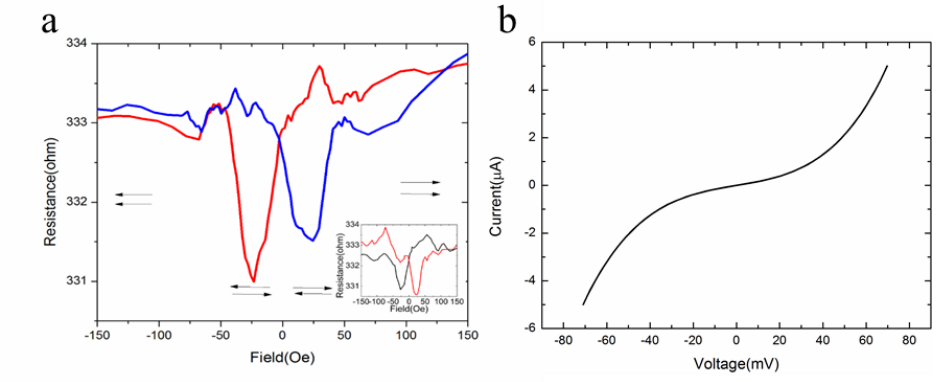


*Fig. 4.3-5(a) MR behavior of LSMO/$MoS_2$/NiFe spin valve device. Inset: MR plot of the same device with applied magnetic field rotated 90$^o$ in the substrate plane. (b) IV curve of the device. All measurements were done at 20 K.*

# Chapter 5. Conclusions and future work

## 5.1. Conclusions

2D TMDs have rapidly developed for use in electronic and optoelectronics. Besides, the spin-related properties of TMD is also outstanding. In this project, we demonstrated the transfer method and deposition process to fabricate spintronic devices based on TMDs. The transfer method allows the preparation of high-quality TMDs flake. However, the limitations of transfer method are the low yield rate, poor contact and high cost for mass production. The deposition method is limited for electrodes or substrates that are stable over 700°C (for CVD) or 450ºC (for sputtered TMD). On the other hand, the direct deposition method produced contaminant-free contacts that are more suitable for mass production.

$MoS_2$ vertical spin valves were fabricated by transfer and deposition $MoS_2$. The transfer $MoS_2$ device show edge contact of bottom and top electrode. LSMO/sputtered $MoS_2$/NiFe spin valve show 0.8% MR ratio at 20 K. The results showed the potential for developing TMD device based on sputtering.

## 5.2. Suggestions for the future work

The spin diffusion length and spin life time of $MoS_2$ was not obtained in the current study. Moreover, the lateral spin valve structure was not available for the calculation of spin properties of $MoS_2$. Further investigations on non-local lateral spin valve should be pursued. Data from non-local lateral spin valve will provide breakthroughs in $MoS_2$ spintronics. [74, 75]

Furthermore, there are some intrinsic ferromagnetic TMDs such as $VSe_2$. [76] They have the potential of 2D spin emitter or spin injector. All-2D material spintronic devices is of great fundamental importance.

# References

[1] W. Han *et al.*, "Tunneling Spin Injection into Single Layer Graphene," *Physical Review Letters,* vol. 105, no. 16, p. 167202, 10/12/ 2010.

[2] T. Y. Yang *et al.*, "Observation of Long Spin-Relaxation Times in Bilayer Graphene at Room Temperature," *Physical Review Letters,* vol. 107, no. 4, p. 047206, 07/21/ 2011.

[3] H. Dery, P. Dalal, L. Cywinski, and L. J. Sham, "Spin-based logic in semiconductors for reconfigurable large-scale circuits," *Nature,* 10.1038/nature05833 vol. 447, no. 7144, pp. 573-6, May 31 2007.

[4] H. Ochoa and R. Roldán, "Spin-orbit-mediated spin relaxation in monolayer MoS2," *Physical Review B,* vol. 87, no. 24, p. 245421, 06/17/ 2013.

[5] K. Dolui, A. Narayan, I. Rungger, and S. Sanvito, "Efficient spin injection and giant magnetoresistance in Fe/MoS2/Fe junctions," *Physical Review B,* vol. 90, no. 4, p. 041401, 07/02/ 2014.

[6] W. Wang *et al.*, "Spin-Valve Effect in NiFe/MoS2/NiFe Junctions," *Nano Lett,* vol. 15, no. 8, pp. 5261-7, Aug 12 2015.

[7] A. Dankert, M. Venkata Kamalakar, A. Wajid, R. S. Patel, and S. P. Dash, "Tunnel magnetoresistance with atomically thin two-dimensional hexagonal boron nitride barriers," *Nano Research,* journal article vol. 8, no. 4, pp. 1357-1364, 2014.

[8] M. Piquemal-Banci *et al.*, "Magnetic tunnel junctions with monolayer hexagonal boron nitride tunnel barriers," *Applied Physics Letters,* vol. 108, no. 10,

p. 102404, 2016.

[9] I. Žutić, J. Fabian, and S. Das Sarma, "Spintronics: Fundamentals and applications," *Reviews of Modern Physics,* vol. 76, no. 2, pp. 323-410, 04/23/ 2004.

[10] N. F. Mott, "The Electrical Conductivity of Transition Metals," *Proceedings of the Royal Society of London. Series A - Mathematical and Physical Sciences,* vol. 153, no. 880, pp. 699-717, 1936.

[11] C. H. Shang, J. Nowak, R. Jansen, and J. S. Moodera, "Temperature dependence of magnetoresistance and surface magnetization in ferromagnetic tunnel junctions," *Physical Review B,* vol. 58, no. 6, pp. R2917-R2920, 08/01/ 1998.

[12] J. Zhang and R. M. White, "Voltage dependence of magnetoresistance in spin dependent tunneling junctions," *Journal of Applied Physics,* vol. 83, no. 11, pp. 6512-6514, 1998.

[13] M. A. Seigler, P. A. A. V. d. Heijden, A. E. Litvinov, and R. E. Rottmayer, "Current-perpendicular-to-plane multilayer sensors for magnetic recording," *IEEE Transactions on Magnetics,* vol. 39, no. 3, pp. 1855-1858, 2003.

[14] J. Bass, "CPP magnetoresistance of magnetic multilayers: A critical review," *Journal of Magnetism and Magnetic Materials,* vol. 408, pp. 244-320, 2016/06/15/ 2016.

[15] S. Mangin, D. Ravelosona, J. A. Katine, M. J. Carey, B. D. Terris, and E. E. Fullerton, "Current-induced magnetization reversal in nanopillars with perpendicular anisotropy," (in English), *Nature Materials,* vol. 5, no. 3, pp. 210-5, Mar 2006.

[16] D. C. Ralph and M. D. Stiles, "Spin transfer torques," *Journal of Magnetism and Magnetic Materials,* vol. 320, no. 7, pp. 1190-1216, 2008/04/01/ 2008.

[17] M. N. Baibich *et al.*, "Giant Magnetoresistance of (001)Fe/(001)Cr Magnetic Superlattices," *Physical Review Letters,* vol. 61, no. 21, pp. 2472-2475, 11/21/ 1988.

[18] B. Dieny, V. S. Speriosu, S. S. P. Parkin, B. A. Gurney, D. R. Wilhoit, and D. Mauri, "Giant magnetoresistive in soft ferromagnetic multilayers," *Physical Review B,* vol. 43, no. 1, pp. 1297-1300, 01/01/ 1991.

[19] S. Ikeda *et al.*, "Tunnel magnetoresistance of 604% at 300K by suppression of Ta diffusion in CoFeB/MgO/CoFeB pseudo-spin-valves annealed at high temperature," *Applied Physics Letters,* vol. 93, no. 8, p. 082508, 2008.

[20] P. M. Tedrow and R. Meservey, "Spin-Dependent Tunneling into Ferromagnetic Nickel," *Physical Review Letters,* vol. 26, no. 4, pp. 192-195, 01/25/ 1971.

[21] F. J. Jedema, A. T. Filip, and B. J. van Wees, "Electrical spin injection and accumulation at room temperature in an all-metal mesoscopic spin valve," *Nature,* 10.1038/35066533 vol. 410, no. 6826, pp. 345-348, 03/15/print 2001.

[22] Z. H. Xiong, D. Wu, Z. Valy Vardeny, and J. Shi, "Giant magnetoresistance in organic spin-valves," *Nature,* 10.1038/nature02325 vol. 427, no. 6977, pp. 821-824, 02/26/print 2004.

[23] M. Julliere, "Tunneling between ferromagnetic films," *Physics Letters A,* vol. 54, no. 3, pp. 225-226, 1975/09/08 1975.

[24] E. Y. Tsymbal and D. G. Pettifor, "Perspectives of giant magnetoresistance," in *Solid State Physics*, vol. Volume 56, E. Henry and S. Frans, Eds.: Academic Press, 2001, pp. 113-237.

[25] W. P. Pratt, S. F. Lee, J. M. Slaughter, R. Loloee, P. A. Schroeder, and J. Bass, "Perpendicular giant magnetoresistances of Ag/Co multilayers," *Physical Review Letters,* vol. 66, no. 23, pp. 3060-3063, 06/10/ 1991.

[26] S. Toshio, S. Tomoyuki, O. Tohru, S. Masashi, S. Yoshishige, and N. Kiyoshi, "Room-Temperature Electron Spin Transport in a Highly Doped Si Channel," *Applied Physics Express,* vol. 4, no. 2, p. 023003, 2011.

[27] X. Lou *et al.*, "Electrical detection of spin transport in lateral ferromagnet-semiconductor devices," *Nat Phys,* 10.1038/nphys543 vol. 3, no. 3, pp. 197-202, 03//print 2007.

[28] N. D. Mermin, "Crystalline Order in Two Dimensions," *Physical Review,* vol. 176, no. 1, pp. 250-254, 12/05/ 1968.

[29] K. S. Novoselov *et al.*, "Electric Field Effect in Atomically Thin Carbon Films," *Science,* vol. 306, no. 5696, pp. 666-669, 2004.

[30] A. D. Yoffe, "Electronic properties of low dimensional solids: The physics and chemistry of layer type transition metal dichalcogenides and their intercalate complexes," *Solid State Ionics,* vol. 39, no. 1, pp. 1-7, 1990/06/01 1990.

[31] RadisavljevicB, RadenovicA, BrivioJ, GiacomettiV, and KisA, "Single-layer MoS2 transistors," *Nat Nano,* 10.1038/nnano.2010.279 vol. 6, no. 3, pp. 147-150, 03//print 2011.

[32] R. Kappera *et al.*, "Phase-engineered low-resistance contacts for ultrathin

MoS2 transistors," *Nat Mater*, Article vol. 13, no. 12, pp. 1128-1134, 12//print 2014.

[33] C. Ataca, H. Sahin, and S. Ciraci, "Stable, Single-Layer MX2 Transition-Metal Oxides and Dichalcogenides in a Honeycomb-Like Structure," (in English), *Journal of Physical Chemistry C*, vol. 116, no. 16, pp. 8983-8999, Apr 26 2012.

[34] A. Castellanos-Gomez, M. Poot, G. A. Steele, H. S. J. van der Zant, N. Agraït, and G. Rubio-Bollinger, "Elastic Properties of Freely Suspended MoS2 Nanosheets," *Advanced Materials*, vol. 24, no. 6, pp. 772-775, 2012.

[35] J. Pu, Y. Yomogida, K.-K. Liu, L.-J. Li, Y. Iwasa, and T. Takenobu, "Highly Flexible MoS2 Thin-Film Transistors with Ion Gel Dielectrics," *Nano Letters*, vol. 12, no. 8, pp. 4013-4017, 2012/08/08 2012.

[36] A. Splendiani *et al.*, "Emerging Photoluminescence in Monolayer MoS2," *Nano Letters*, vol. 10, no. 4, pp. 1271-1275, 2010/04/14 2010.

[37] C. Lee, H. Yan, L. E. Brus, T. F. Heinz, J. Hone, and S. Ryu, "Anomalous Lattice Vibrations of Single- and Few-Layer MoS2," *ACS Nano*, vol. 4, no. 5, pp. 2695-2700, 2010/05/25 2010.

[38] Y. Lin and J. W. Connell, "Advances in 2D boron nitride nanostructures: nanosheets, nanoribbons, nanomeshes, and hybrids with graphene," *Nanoscale*, 10.1039/C2NR32201C vol. 4, no. 22, pp. 6908-6939, 2012.

[39] S. J. Haigh *et al.*, "Cross-sectional imaging of individual layers and buried interfaces of graphene-based heterostructures and superlattices," *Nat Mater*, 10.1038/nmat3386 vol. 11, no. 9, pp. 764-767, 09//print 2012.

[40] L. A. Ponomarenko *et al.*, "Tunable metal-insulator transition in double-

layer graphene heterostructures," *Nat Phys,* 10.1038/nphys2114 vol. 7, no. 12, pp. 958-961, 12//print 2011.

[41] T. Georgiou *et al.,* "Vertical field-effect transistor based on graphene-WS2 heterostructures for flexible and transparent electronics," *Nat Nano,* 10.1038/nnano.2012.224 vol. 8, no. 2, pp. 100-103, 02//print 2013.

[42] Y. Yao, Z. Lin, Z. Li, X. Song, K.-S. Moon, and C.-p. Wong, "Large-scale production of two-dimensional nanosheets," *Journal of Materials Chemistry,* 10.1039/C2JM30587A vol. 22, no. 27, pp. 13494-13499, 2012.

[43] J. N. Coleman *et al.,* "Two-Dimensional Nanosheets Produced by Liquid Exfoliation of Layered Materials," *Science,* vol. 331, no. 6017, pp. 568-571, 2011.

[44] G. Eda, H. Yamaguchi, D. Voiry, T. Fujita, M. Chen, and M. Chhowalla, "Photoluminescence from Chemically Exfoliated MoS2," *Nano Letters,* vol. 11, no. 12, pp. 5111-5116, 2011/12/14 2011.

[45] Z. Zeng *et al.,* "Single-Layer Semiconducting Nanosheets: High-Yield Preparation and Device Fabrication," *Angewandte Chemie International Edition,* vol. 50, no. 47, pp. 11093-11097, 2011.

[46] S. Najmaei *et al.,* "Vapour phase growth and grain boundary structure of molybdenum disulphide atomic layers," *Nat Mater,* Article vol. 12, no. 8, pp. 754-759, 08//print 2013.

[47] Y.-C. Lin *et al.,* "Wafer-scale MoS2 thin layers prepared by MoO3 sulphurization," *Nanoscale,* 10.1039/C2NR31833D vol. 4, no. 20, pp. 6637-6641, 2012.

[48] M. E. McConney *et al.,* "Direct synthesis of ultra-thin large area transition

metal dichalcogenides and their heterostructures on stretchable polymer surfaces," *Journal of Materials Research,* vol. 31, no. 7, pp. 967-974, 2016/004/14 2016.

[49] J. Tao *et al.*, "Growth of wafer-scale MoS2 monolayer by magnetron sputtering," *Nanoscale,* 10.1039/C4NR06411A vol. 7, no. 6, pp. 2497-2503, 2015.

[50] M. I. Serna *et al.*, "Large-Area Deposition of MoS2 by Pulsed Laser Deposition with In Situ Thickness Control," *ACS Nano,* vol. 10, no. 6, pp. 6054-6061, 2016/06/28 2016.

[51] J. Cervenka, M. I. Katsnelson, and C. F. J. Flipse, "Room-temperature ferromagnetism in graphite driven by two-dimensional networks of point defects," *Nat Phys,* 10.1038/nphys1399 vol. 5, no. 11, pp. 840-844, 11//print 2009.

[52] R. R. Nair *et al.*, "Spin-half paramagnetism in graphene induced by point defects," *Nat Phys,* 10.1038/nphys2183 vol. 8, no. 3, pp. 199-202, 03//print 2012.

[53] O. V. Yazyev and L. Helm, "Defect-induced magnetism in graphene," *Physical Review B,* vol. 75, no. 12, p. 125408, 03/08/ 2007.

[54] K. F. Mak, K. He, J. Shan, and T. F. Heinz, "Control of valley polarization in monolayer MoS2 by optical helicity," *Nat Nano,* 10.1038/nnano.2012.96 vol. 7, no. 8, pp. 494-498, 08//print 2012.

[55] B. Bishnoi and B. Ghosh, "Spin transport in monolayer molybdenum disulfide (MoS2)," *Journal of Computational Electronics,* journal article vol. 13, no. 2, pp. 394-399, 2014.

[56] "Preparation of Y-Ba-Cu oxide superconductor thin films using pulsed laser evaporation from high Tc bulk material," *Applied Physics Letters,* vol. 51, no. 8, pp. 619-621, 1987/08/24 1987.

[57] M. R. R. Vaziri, F. Hajiesmaeilbaigi, and M. H. Maleki, "Microscopic description of the thermalization process during pulsed laser deposition of aluminium in the presence of argon background gas," (in English), *Journal of Physics D-Applied Physics*, vol. 43, no. 42, p. 425205, Oct 27 2010.

[58] X. Zhang, X.-F. Qiao, W. Shi, J.-B. Wu, D.-S. Jiang, and P.-H. Tan, "Phonon and Raman scattering of two-dimensional transition metal dichalcogenides from monolayer, multilayer to bulk material," *Chemical Society Reviews*, 10.1039/C4CS00282B vol. 44, no. 9, pp. 2757-2785, 2015.

[59] Y. Zhao *et al.*, "Interlayer Breathing and Shear Modes in Few-Trilayer MoS2 and WSe2," *Nano Letters*, vol. 13, no. 3, pp. 1007-1015, 2013/03/13 2013.

[60] F. Schedin *et al.*, "Surface-Enhanced Raman Spectroscopy of Graphene," *ACS Nano*, vol. 4, no. 10, pp. 5617-5626, 2010/10/26 2010.

[61] N. Jalili and K. Laxminarayana, "A review of atomic force microscopy imaging systems: application to molecular metrology and biological sciences," *Mechatronics*, vol. 14, no. 8, pp. 907-945, 10// 2004.

[62] A. A. Bunaciu, E. g. Udriştioiu, and H. Y. Aboul-Enein, "X-Ray Diffraction: Instrumentation and Applications," *Critical Reviews in Analytical Chemistry*, vol. 45, no. 4, pp. 289-299, 2015/10/02 2015.

[63] S. Foner, "Vibrating Sample Magnetometer," *Review of Scientific Instruments*, vol. 27, no. 7, pp. 548-548, 1956/07/01 1956.

[64] C.-G. Andres *et al.*, "Deterministic transfer of two-dimensional materials by all-dry viscoelastic stamping," *2D Materials*, vol. 1, no. 1, p. 011002, 2014.

[65] J. Jeon *et al.*, "Layer-controlled CVD growth of large-area two-

dimensional MoS2 films," *Nanoscale,* 10.1039/C4NR04532G vol. 7, no. 5, pp. 1688-1695, 2015.

[66] H. F. Liu, S. L. Wong, and D. Z. Chi, "CVD Growth of MoS2-based Two-dimensional Materials," *Chemical Vapor Deposition,* vol. 21, no. 10-11-12, pp. 241-259, 2015.

[67] H. Li *et al.*, "From Bulk to Monolayer MoS2: Evolution of Raman Scattering," *Advanced Functional Materials,* vol. 22, no. 7, pp. 1385-1390, 2012.

[68] A. L. Friedman, O. M. J. van ‘t Erve, C. H. Li, J. T. Robinson, and B. T. Jonker, "Homoepitaxial tunnel barriers with functionalized graphene-on-graphene for charge and spin transport," *Nature Communications,* Article vol. 5, p. 3161, 01/21/online 2014.

[69] W. Han *et al.*, "Electrical detection of spin precession in single layer graphene spin valves with transparent contacts," *Applied Physics Letters,* vol. 94, no. 22, p. 222109, 2009.

[70] M. Popinciuc *et al.*, "Electronic spin transport in graphene field-effect transistors," *Physical Review B,* vol. 80, no. 21, p. 214427, 12/30/ 2009.

[71] J. G. Connell, B. J. Isaac, G. B. Ekanayake, D. R. Strachan, and S. S. A. Seo, "Preparation of atomically flat SrTiO3 surfaces using a deionized-water leaching and thermal annealing procedure," *Applied Physics Letters,* vol. 101, no. 25, p. 251607, 2012.

[72] J. R. Sun, H. W. Yeung, H. K. Wong, T. Zhu, and B. G. Shen, "Effects of vacuum annealing on the transport property of La0.67Sr 0.33MnO3-δ films," *Eur. Phys. J. B,* vol. 35, no. 4, pp. 481-491, 2003.

[73] H. M. Yau *et al.*, "Low-field Switching Four-state Nonvolatile Memory Based on Multiferroic Tunnel Junctions," *Scientific Reports,* Article vol. 5, p. 12826, 08/04/online 2015.

[74] W. Han, "Perspectives for spintronics in 2D materials," *APL Materials,* vol. 4, no. 3, p. 032401, 2016/03/01 2016.

[75] N. Zibouche, A. Kuc, J. Musfeldt, and T. Heine, "Transition-metal dichalcogenides for spintronic applications," *Annalen der Physik,* vol. 526, no. 9-10, pp. 395-401, 2014.

[76] F. Li, K. Tu, and Z. Chen, "Versatile Electronic Properties of VSe2 Bulk, Few-Layers, Monolayer, Nanoribbons, and Nanotubes: A Computational Exploration," *The Journal of Physical Chemistry C,* vol. 118, no. 36, pp. 21264-21274, 2014/09/11 2014.